JOURNAL OF AIRCRAFT
Vol. 46, No. 2, March–April 2009

Lessons Learned from Numerical Simulations of the F-16XL Aircraft at Flight Conditions

Arthur Rizzi*
Royal Institute of Technology, 100 44 Stockholm, Sweden
Adam Jirásek†
Swedish Defence Research Agency, 164 90 Stockholm, Sweden
John E. Lamar‡
NASA Langley Research Center, Hampton, Virginia 23681
Simone Crippa§
Royal Institute of Technology, 100 44 Stockholm, Sweden
Kenneth J. Badcock¶
University of Liverpool, Liverpool, England L69 3GH, United Kingdom
and
Okko J. Boelens**
National Aerospace Laboratory/NLR, 1059 CM Amsterdam, The Netherlands

DOI: 10.2514/1.35698

Nine organizations participated in the Cranked-Arrow Wing Aerodynamics Project International study and have contributed steady and unsteady viscous simulations of a full-scale semispan model of the F-16XL aircraft. Three different categories of flight Reynolds/Mach number combinations are computed and compared with flight-test measurements for the purpose of code validation and improved understanding of the flight physics. Steady-state simulations are done with several turbulence models (of different complexity, with no topology information required) that overcome Boussinesq-assumption problems in vortical flows. Detached-eddy simulation and its successor, delayed detached-eddy simulation, are used to compute the time-accurate flow development. Common structured and unstructured grids as well as individually adapted unstructured grids were used. Although discrepancies are observed in the comparisons, overall reasonable agreement is demonstrated for surface pressure distribution, local skin friction, and boundary velocity profiles at subsonic speeds. The physical modeling, be it steady or unsteady flow, and the grid resolution both contribute to the discrepancies observed in the comparisons with flight data, but at this time, how much each part contributes to the whole cannot be determined. Overall, it can be said that the technology readiness of computational fluid dynamics simulation technology for the study of vehicle performance has matured since 2001, such that it can be used today with a reasonable level of confidence for complex configurations.

Nomenclature

C_D	=	drag coefficient
C_{D_f}	=	drag coefficient, friction part
C_L	=	lift coefficient
C_M	=	pitching moment
C_p	=	static-pressure coefficient
C_p^*	=	static-pressure coefficient at critical condition
C_Y	=	rolling moment coefficient
C_Z	=	yawing moment coefficient
$\mathbf{c}_f$	=	local skin-friction coefficient vector, $\tau_w/0.5\rho V_\infty^2$
$k\hat{\sigma}$	=	estimate of population standard deviation
M_∞	=	flight Mach number
Re	=	Reynolds number
V/V_{RE}	=	ratio of velocity magnitude in the boundary layer to that at the rake extreme total-pressure tube
x/c	=	fractional distance along the local chord
y^+	=	dimensionless sublayer-scale distance, $u_\tau y/\nu$
$2y/b_{\mathrm{local}}$	=	fractional distance along the local semispan, positive toward the right wing tip
α	=	angle of attack
λ_2	=	second eigenvalue of the $\mathbf{S}$-Ω tensor
$\hat{\mu}$	=	estimate of the population mean

Presented as Paper 683 at the 45th AIAA Aerospace Sciences Meeting and Exhibit, Reno, NV, 8–11 January 2007; received 15 November 2007; revision received 11 December 2008; accepted for publication 18 April 2008.

*Professor of Aeronautics, Department of Aeronautical and Vehicle Engineering. Associate Fellow AIAA.
†Research and Development Engineer, Division of Systems Technology. Member AIAA.
‡CAWAP Principal Investigator, Retired. Associate Fellow AIAA.
§Research Assistant, Department of Aeronautical and Vehicle Engineering. Student Member AIAA.
¶Professor of Computational Aerodynamics, Department of Engineering, AIAA Member
**Research and Development Engineer, Applied Computational Fluid Dynamics, Department of Flight Physics and Loads, Aerospace Vehicles Division. Member AIAA.

I. Introduction

THE original NASA document [1] together with [2] introduced the problem that the AVT-113 task group studied: that of increasing the Technology Readiness Level (TRL) of the CFD solvers by establishing best practices with the solvers as applied to the F-16XL aircraft at a number of flight conditions. Reference [3] reported how the grids were established for each solver type (structured, unstructured common, or tailored) or with a particular solver studied, and the remaining companion papers [4–6] in this series presented analyses and representative results for each solver type. This paper draws from the base papers [7–16], presented at two special sessions of the AIAA Aerospace Sciences Meeting in January 2007, along with new analysis and summaries, not

previously available, to put into perspective what was accomplished by the Cranked-Arrow Wing Aerodynamics Project International (CAWAPI) facet of the AVT-113 task group. Moreover, CFD comparisons are also offered with those reported in the basic document [1], which was used to launch this study.

This paper cumulatively compares all of the computed results with the flight-test measurements, makes some overall observations about these comparisons, discusses some likely causes for discrepancies, and, when possible, draws tentative conclusions and tries to identify lessons learned to take a step forward toward establishing some best practices for this class of problem. Similar cumulative-comparison activities have been done before, notably among them, the series of AIAA Drag Prediction Workshops. What we do here differs in that it is a fighter configuration, a flying aircraft, and the comparisons are done against flight-test data, not wind-tunnel measurements, which makes it rather unique. Furthermore, the objective is not the accurate prediction of, say, total drag counts, but instead is the prediction of complex vortical-flow phenomena that strongly impact the flying qualities of a fighter aircraft, because the interaction of vortices over such an aircraft determines its stability and control characteristics.

The lessons learned in this five-year study are reported here by first reviewing the impact of the grid on the CFD solvers and the ensuing solutions, then the predictive capabilities themselves of the solvers for selected dominant vortical- and transonic-flow flight conditions, along with any deficiencies, are noted. The flight condition (FC) at the highest angle of attack (FC25) is discussed using three sets of representative results. This case showed significant unsteady flow. For FC19, results are compared for the prediction of skin-friction and for boundary-layer profiles in FC7. Next, a wide-ranging effort to explain significant discrepancies between measurements and computations for the transonic flight condition (FC70) is described. A high-level overall assessment is then made by first comparing progress achieved since the NASA publication [1] from 2001 and then by quoting comments made by industry participants regarding the value of their participation in the study. Finally, conclusions are stated.

CFD solutions used in this study can be postprocessed to predict not only surface flow physics, but also the component force and moment coefficients for the aircraft. Appendix A provides a comparison of these coefficients from the different solvers, along with a simple statistical analysis of the predicted data, and Appendix B details the means by which the statistical analysis was performed.

II. Overview of Codes and Comparisons

Table 1 lists the 10 solvers used in CAWAPI, along with a brief description of relevant information about each, including the models employed, whether steady or unsteady flow was computed, and the grid type used. The flight conditions computed by each partner are also listed. The geometry used during this exercise is a detailed model of the F-16XL geometry. Details on both geometry and grids are reported by Lamar et al. [1], Obara and Lamar [2], and Boelens et al. [3]. More details on the solvers can be found in [4–6]. Note that all turbulence models integrate to the wall, with the exception of the Lockheed Martin Aeronautics Company (LM Aero) model, which used wall functions. The rows in the table are grouped by the grid type used. The first group used a common multiblock grid, the second group used a common unstructured grid, and the third group used tailored grids, referred to in this paper as trimmed grids. The flight conditions are defined in detail by Obara and Lamar [2].

In this paper, the conditions computed are split into two groups. The first (FC7, FC19, FC25, FC46, FC50, and FC51) are dominated by strong vortices and have low subsonic freestream Mach numbers at moderate-to-high angles of attack. The second group (FC70) is at high subsonic freestream Mach numbers and a relatively low angle of attack, and it features shock waves and a weak vortex. The comparisons are made separately for these two groups of conditions.

III. Low-Speed-Flow Cases

A. Unsteady Flow at High Angle of Attack: FC25

1. Overview

The conditions for FC25 are $M_\infty = 0.242$, $\alpha = 19.8$ deg, and $Re = 32.22 \times 10^6$. FC25 has the largest angle of attack, and thus better defined vortical-flow phenomena are expected over the upper surface, perhaps even vortex breakdown over the aft portion of the aircraft. Large-scale flow unsteadiness is also associated with such phenomena. For this flight condition, surface pressure measurements are available.

Table 1 Overview of 10 solutions generated by the nine participating organizations

Contributor	Grid type	Turbulence models[a]	Numerics[b]	FC
NLR [7,17] ENFLOW	Common structured	k-ω and vorticity corrections	CC, central	FC7, FC19, FC25, FC46, FC50, FC51, FC70
University of Liverpool [9] PMB	Common structured	k-ω TNT and vorticity corrections	CC, Osher upwind, Roe flux-vector splitting	FC7, FC19, FC25, FC46, FC70
LaRC [10] PAB3D	Common structured	k-ω, SZL EARSM, Girimaji EARSM	CC, Roe flux-vector splitting, implicit 3 factor scheme, explicit: DTS	FC7, FC19, FC25, FC46, FC50, FC51, FC70
USAFA [15] Cobalt	Common unstructured	SARC-DES[d], SARC-DDES	CC, Godunov type with least-squares approximation, implicit with Newton method	FC7[c], FC19[c], FC25[c], FC46[c], FC50[c], FC51,[c] FC70[c]
KTH/FOI [11] Edge	Common and trimmed unstructured	SA, Hellsten EARSM k-ω[a], Hellsten EARSM k-ω and rotational corrections, DES, hybrid RANS-LES	NC, central	FC7[c], FC19, FC25[c], FC46[c], FC50, FC51, FC70 (Euler, RANS)
LaRC [14] USM3D	Common unstructured	Linear k-ϵ[a], nonlinear k-ϵ	CC, Roe FDS, implicit scheme	FC7, FC19, FC25, FC46, FC50, FC51, FC70
EADS-MAS [12] Tau	Trimmed unstructured	SA	NC, AUSMDV, backward Euler implicit, and LU-SGS	FC7, FC19, FC25, FC46, FC50, FC51, FC70
UTSimCenter [13] TENASI	Trimmed unstructured	k-ω/k-ϵ hybrid	NC, Roe flux-vector splitting, point implicit	FC7, FC19, FC25, FC46, FC50, FC51, FC70
Boeing [8] BCFD	Trimmed unstructured	SA, Menter SST, SST-LESb	CC, HLLE, FDS	FC7[c], FC19, FC25[c], FC46, FC70
LM Aero [16] Falcon v.4	Trimmed unstructured	k-kl	Roe approximate Riemann solver, implicit ILU	FC7, FC19, FC70

[a]TNT: turbulent/nonturbulent, SZL: Shih–Zhu–Lumley; SA: Spalart-Allmaras; SST: shear stress transport; DTS: dual time stepping; FDS: flux difference splitting; HLLE: Harten, Van Leer, Lax, and Enfield; LU-SGS: lower/upper symmetric Gauss–Seidel; and ILU: incomplete lower/upper factorization.
[b]Numerical method cell-centered (CC) or node-centered (NC).
[c]Flight condition calculated as unsteady.
[d]Turbulence model used in common comparisons.

2. Vortical-Flow Features

Figure 1 presents sectional spanwise contours of iso-total-pressure, skin-friction lines, and flight tuft patterns. The contour plots indicate the presence and location of the inner-wing primary and secondary vortices and the outer-wing primary and secondary vortices. The convergence–divergence of skin-friction lines indicates the occurrence and location of primary- or secondary-vortex separation–reattachment, respectively. Figure 1b suggests that the separation layer on the fuselage is now drawn outboard toward the actuator pod, in which it may merge with the vortical flow around that structure. There are striking overall similarities with the in-flight photographs of the tufts shown in Fig. 1c. Similar behavior is observed for the inward flow to the air dam on both the inner and outer wings and the marked flow division that occurs on the outer wing. Differences are seen for the inner-wing spanwise flow extending toward the fuselage, especially near the trailing edge.

3. C_p Comparisons Along Butt-Line Sections

A downselect of the 10 solutions makes the FC25 C_p comparison with flight data more tractable. One solution from each type of grid was selected: namely, National Aerospace Laboratory/NLR (NLR) for the standard structured grid; European Aeronautics and Defence Company, Military Aircraft Systems (EADS) for the tailored unstructured grid; and U.S. Air Force Academy (USAFA) for the standard unstructured grid. Keep in mind that the first two results are steady-state Reynolds-averaged Navier–Stokes (RANS) solutions, whereas the third (USAFA) is a time-accurate detached-eddy simulation (DES) solution [15]. These three results have been cross-plotted with the flight data, and the previous CFL3D solutions [1] and their comparisons are now shown. The time-averaged value (mean) is plotted for the unsteady USAFA solution. Görtz et al. [5] reported significant unsteadiness in their solutions located over the rear of the wing, close to the wing tip, especially at BL184.5.

Figure 2 shows comparisons of the computed and flight-measured surface pressure coefficients C_p plotted along the butt lines, the first four along the inner wing, and the last two along the outer wing, where we expect strong interactions. The first four butt lines (BL55, BL70, BL80, and BL95) show that the pressures associated with inner-wing primary and secondary vortices are being resolved. The leading-edge vortex forms in the vicinity of BL55, and the measured values show a primary-vortex peak as well as a secondary-vortex peak, as do some, but not all, of the computed results. The falloff in primary suction peak from BL55 to BL95 is associated with the center of the vortex system moving further from the surface as the system travels further downstream. This feature is caused by the system capturing more leading-edge shed vorticity as it traverses the wing, yielding an enlarged cross section. Morton et al. [15] presented similar inner butt-line plots of the instantaneous values of minimum and maximum C_p that forms a band around the time-averaged mean values. Over the inner wing, this band is very thin, indicating that the flow here is steady.

At BL153.5 and BL184.5, the predicted and measured pressures demonstrate that there are strong interactions between the vortices shed from the inner wing, actuator pod, air dam, and crank. At BL153.5, just outboard of the juncture of these vortices, the computed and measured results show a suction peak for the outer-wing primary vortex near 15% chord and a smaller peak near 75% chord from the combination of actuator-pod/air-dam/inner-wing secondary vortices; however, the predictions for the second peak have something of a spread in the peak value and its location. At BL184.5, the measured peak value for the outer-wing primary vortex is much reduced and its location occurs closer the leading edge, near 10% chord. A second smaller peak is predicted to occur at this butt line near midchord and is primarily associated with the inner-wing secondary vortex (see Fig. 1b). Note that the flow in the vicinity of the wing tip is made even more complicated because of the vortex wake off of the missile fins, especially at this angle of attack. For these two butt-line locations on the outer wing, the plot by Morton et al. [15]

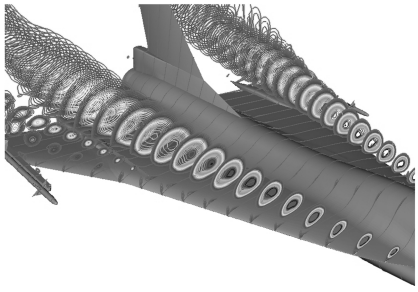

a) Sectional spanwise iso-total-pressure contours [7]

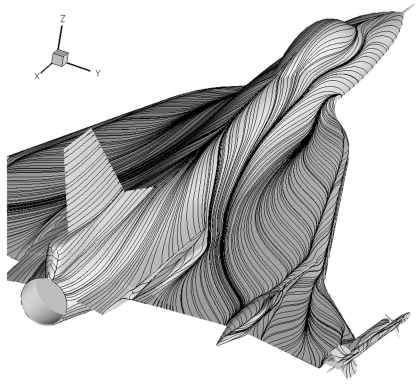

b) Skin friction lines [7]

c) Flight tuft photo from vertical-tail top-left camera mirrored about the vertical axis of the photo [1]

Fig. 1 Vortical-flow features over the upper surface for FC25.

shows bands between the minimum and maximum instantaneous C_p values that are very broad and encompass the measured data. This indicates that the flow over the outboard wing section has substantial unsteadiness. It also suggests that the USAFA mean value plotted in Figs. 2e and 2f is a more accurate estimate of the unsteady pressure distribution than the other Reynolds-averaged steady-state results.

From the comparisons presented, the solver used by USAFA with the DES turbulence model produced the best overall agreement with the flight data, indicating that for this angle of attack, modeling the large-scale unsteadiness in a time-accurate mode is a key to improved predictability. All of the new solvers showed superior agreement with data in comparison with that documented by Lamar et al. [1] and Obara and Lamar [2] for the CFL3D solver with an order-of-magnitude-fewer grid points used and a larger y^+ value.

B. Skin-Friction Coefficient: FC19

1. *Overview*

The conditions for FC19 are $M_\infty = 0.36$, $\alpha = 11.85$ deg, and $Re = 46.8 \times 10^6$. FC19 is also a case of fully developed vortical flow over the upper surface. For this flight condition, skin-friction measurements are available.

2. *Vortical-Flow Features*

Figure 3 shows sectional spanwise contours of iso-total-pressure and skin-friction lines. The contour plots indicate the presence and location of the inner-wing primary and secondary vortices and the outer-wing primary and secondary vortices. Note the presence of small fuselage vortices that were not present for FC25 (see Fig. 1).

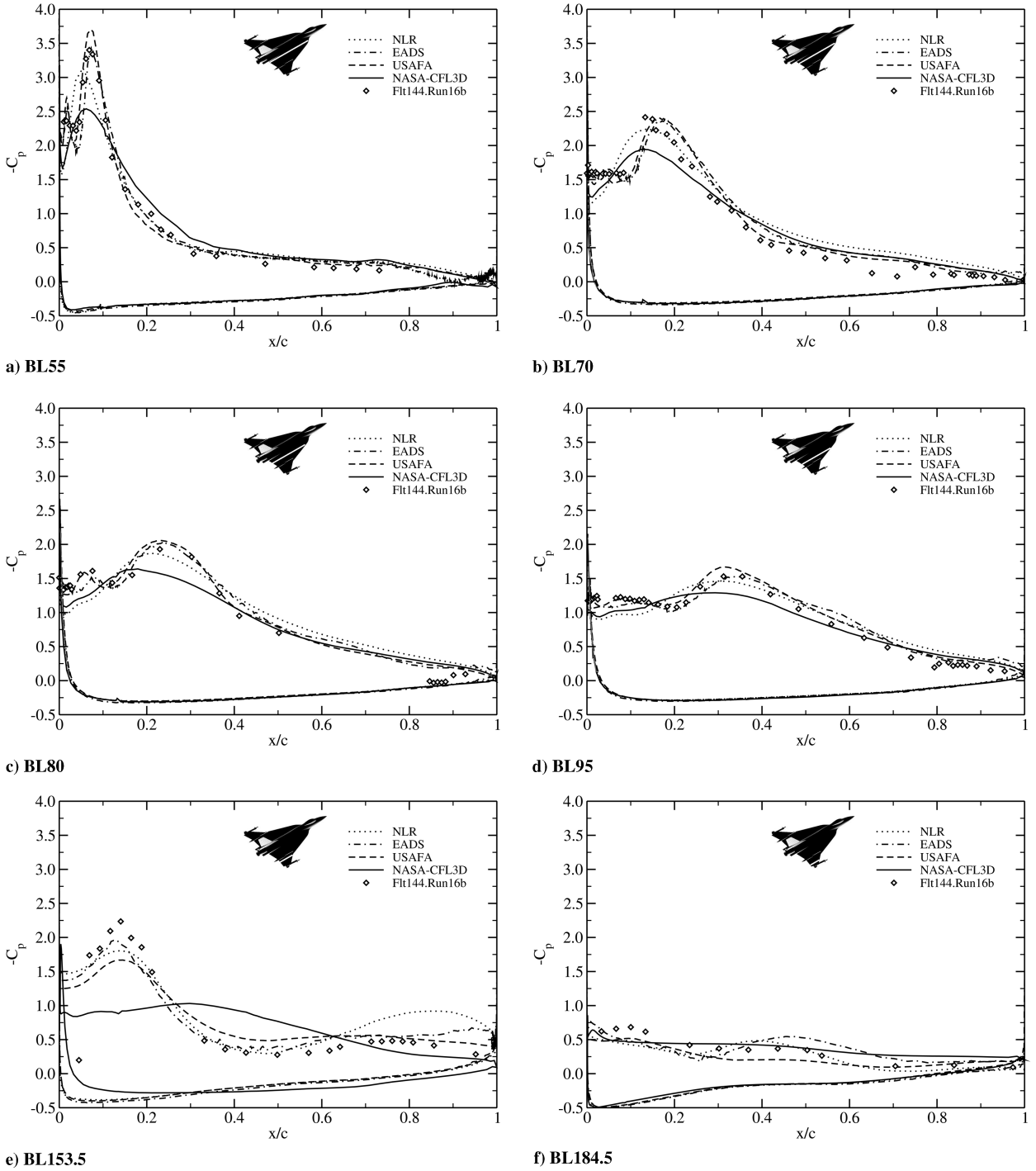

Fig. 2 Chordwise comparison for FC25 of pressure coefficient; see Table 1 for the solutions provided by the listed organizations; solutions for NASA-CFL3D [1] were obtained at LaRC.

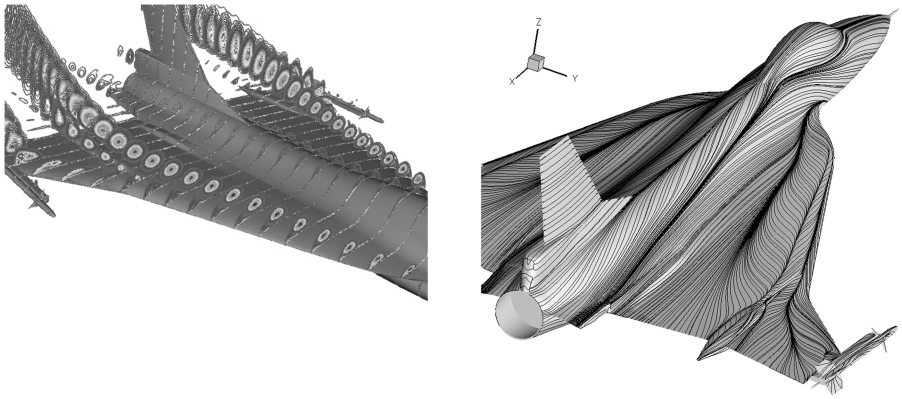

a) Sectional spanwise iso-total-pressure contours [7] b) Skin friction lines [7]

Fig. 3 Vortical-flow features over the upper surface for FC19.

3. Skin-Friction Comparison

Figure 4 compares the computed and measured values of the skin-friction coefficient c_f at fuselage station FS330. In general, the skin-friction coefficient c_f is a vector quantity. The measurements were made with modified Preston tubes that pointed into the local flow direction, which varied across the FS330. The fact that the local skin friction can be correlated with the Δp between the static and total pressure is the basis of these measurements. The comparison is made with the magnitude of the computed vector quantity. The location FS330 is in the general vicinity of the boundary-layer rakes discussed subsequently. The measured values show two peaks in c_f: the highest under the primary inner-wing vortex and the lowest under the secondary inner-wing vortex. There is another peak noted in some of the solutions near $2y/b_{\text{local}} \sim 0.5$ and it is associated with a small surface geometrical feature omitted in most grids. The computed results of the Royal Institute of Technology (KTH), Swedish Defence Research Agency (FOI), and NASA Langley Research Center (LaRC) unstructured solvers show three peaks; the inboard peak occurs at a location in which there are no measurements that could confirm it. USAFA results, which were obtained on the same mesh, do not show the third peak. It is clearly visible that trimmed unstructured-mesh results [EADS and Boeing-Phantom Works (Boeing)] give almost identical results.

C. Velocity Profiles: FC7

1. Overview

FC7 has conditions $M_\infty = 0.304$, $\alpha = 11.89$ deg, and $Re = 44.4 \times 10^6$. These are similar to FC19, and the flow topology is also similar. For this case, boundary-layer measurements are available.

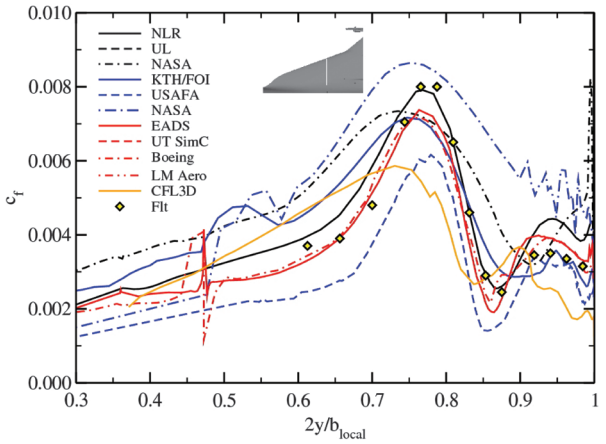

Color coding: Black - Common structured mesh
Blue - Common unstructured mesh
Red - Trimmed unstructured mesh

Fig. 4 Spanwise comparison (FS330) for FC19 of the magnitude of the skin-friction coefficient c_f; see Table 1 for the solutions provided by the listed organizations; UL denotes the University of Liverpool.

2. Velocity Comparisons

Figure 5 shows the comparison of measured and predicted boundary-layer profiles for rake locations 3, 4, 5 and 7 for all RANS solutions [7–14,16], USAFA delayed detached-eddy simulation (DDES) [15], and CFL3D results [1]. The agreement with flight-test data is very good for three of four positions (3, 4, and 5). In position 7, the spread of all results is rather large. Some of the results show jet-type flow (USAFA and LaRC unstructured solvers). On the other side is EADS, which predicts lower velocities. This rake is located underneath the separation line between the primary and secondary vortex, and so the flow is complicated in this region. Inspection of the results shows that the structured-mesh results have the smallest spread, especially in positions 5 and 7, compared with other results. The largest spread is in the common unstructured results.

A comparison of steady-vs-unsteady results is also interesting. Figure 6 shows the envelope of velocity profiles for all RANS solutions in black, with unsteady DES, DDES, and hybrid RANS-LES (large eddy simulation) of USAFA and KTH/FOI [5] in two positions in which comparisons are the most interesting: positions 5 and 7. The scatter between RANS data at position 5 (Fig. 6a) is large, which is also true for different unsteady methodologies. The KTH/FOI DES result shows the largest deviation to the average result, whereas the USAFA DES lies on the boundary of RANS model's interval. USAFA DDES and KTH/FOI hybrid modeling move velocity profiles closer to flight-test data and into the cloud of RANS results. The results at rake 7, shown in Fig. 6b, have large scatter. The KTH/FOI hybrid model shows good agreement with flight data. The DES-model-predicted velocity profile is on the boundary of the RANS results envelope. USAFA deviates from other results, showing substantial improvement of the DDES over DES methodology.

The DES results have trouble predicting velocity profiles in regions of highly stretched cells. One possible reason for this could be that the DES model does not use RANS in the boundary layer, but switches to LES because the grid is so refined in the streamwise direction, resulting in a false log layer. Because the outer edge condition is used in the scaling for the comparisons, this can result in the jetlike profile seen in the USAFA results. The DDES model forces the solver to stay in a RANS mode in the boundary layer, even with refined grids in the boundary layer. These rakes are placed very close to the leading edge, with a very refined grid to capture the leading-edge suction peaks, and are therefore susceptible to this problem. The overall pressure results are fairly insensitive to this, but the boundary-layer rake data and skin-friction DES results seem to be suffering from the problem. The DDES model improves the situation for rake 5, but less so for rake 7.

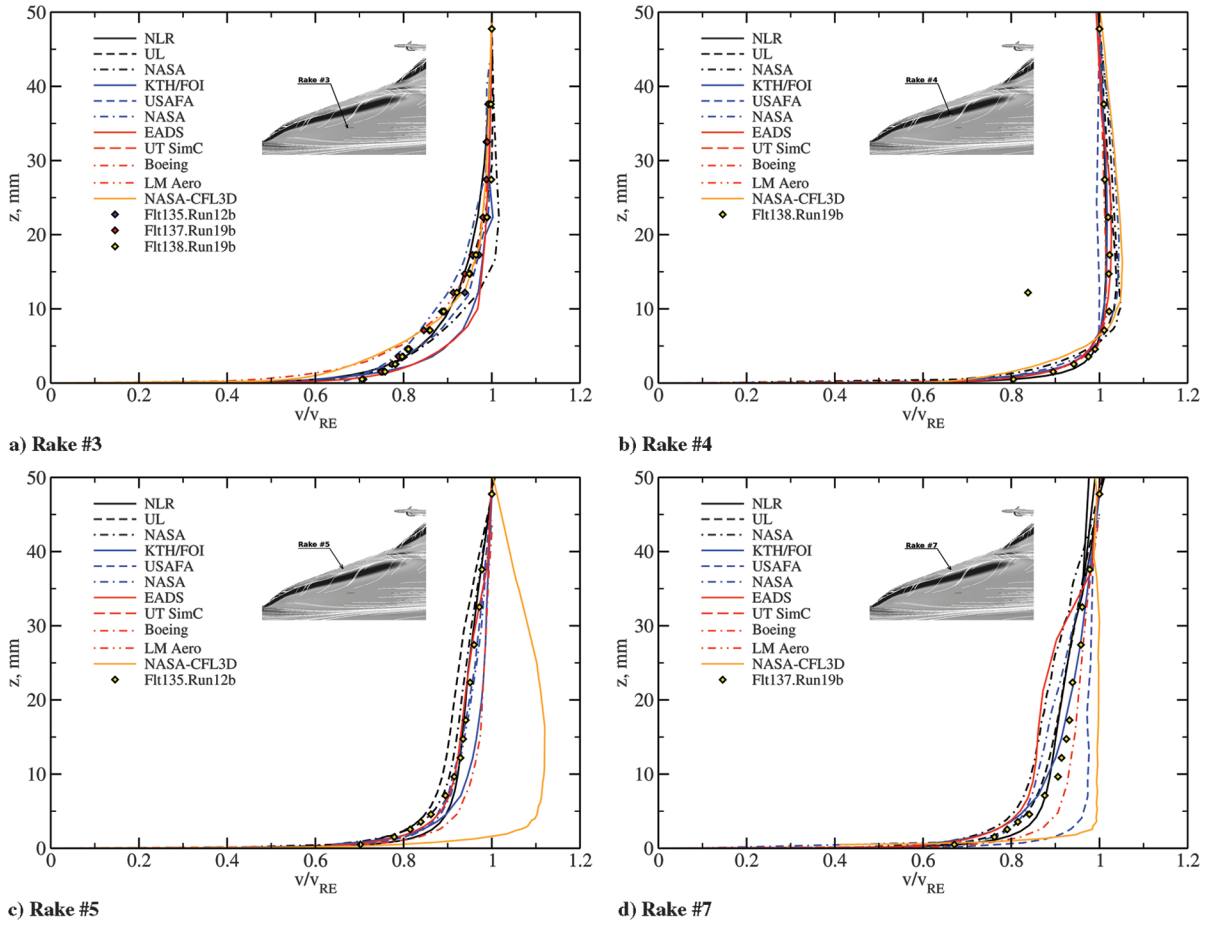

Fig. 5 FC7 velocity profile comparison; see Table 1 for the solutions provided by the listed organizations; LMAC denotes Lockheed Martin Aeronautics Company.

D. Results at Sideslip Flight Conditions: FC50 and FC51

Two additional flight conditions are sideslip conditions at angle of attack around $\alpha = 13$ deg and subsonic Mach numbers around $M = 0.44$ and $Re = 39 \times 10^6$. These two conditions denoted as FC50 and FC51 have the values of sideslip angle $\beta = 5.31$ deg (FC50) and $\beta = -4.58$ deg (FC51). The effect of a sideslip angle is to decrease the effective leading-edge sweep angle of the windward-side wing and to increase the leading-edge sweep angle of the leeward-side wing. This effective decrease of sweep angle may cause vortex breakdown on the windward side to occur at a lower angle of attack than it would occur with no sideslip. In addition, the reduced sweep angle may cause a double-vortex structure [18]. These two flight conditions were not a main focus of the CAWAPI team. Two cases were, however, computed by some partners. Görtz et al. [5] reported on a study that outlines the effect of turbulence models and unsteadiness of the solution, which seems to be significant for BL70 up to BL184.5.

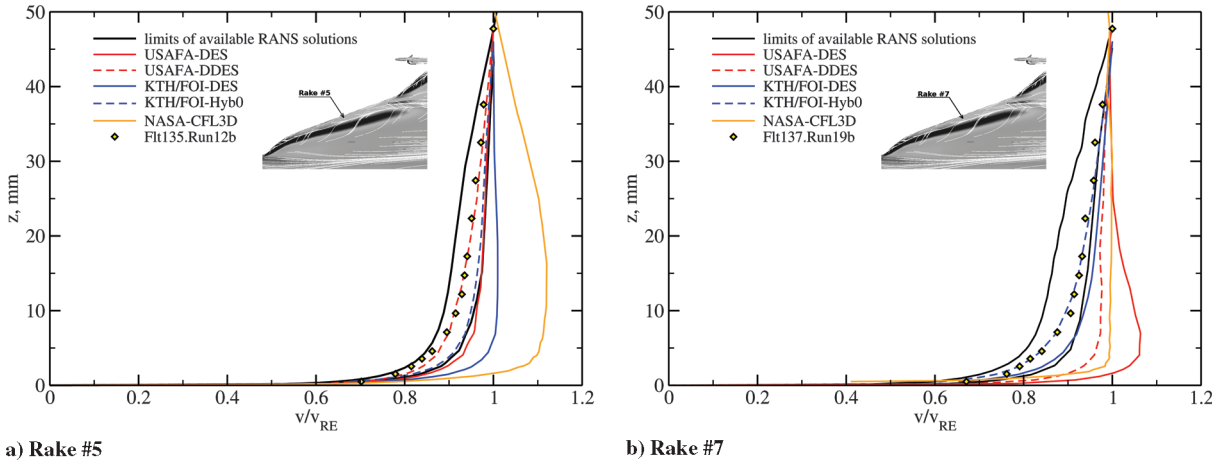

Fig. 6 FC7 velocity profiles comparison; effect of turbulence modeling and time-accuracy; see Table 1 for the solutions provided by the listed organizations.

IV. Transonic Flow Case

A. Overview

FC70 has conditions $M_\infty = 0.97$, $\alpha = 4.3$ deg, and $Re = 88.8 \times 10^6$. This condition has the smallest angle of attack of all of the test flights considered and a high subsonic freestream Mach number. Hence, reduced-strength vortical-flow phenomena over the upper surface and strong transonic effects are expected. It must be pointed out that there is some degree of uncertainty in the flight-test data concerning whether, and how much, a flap was deflected during the measurements. Transonic effects are also very sensitive to flight conditions, and even weak interactions can lead to substantial changes in flow structure.

B. Overall Vortical-Flow Features

Figure 7 presents sectional spanwise contours of iso-total-pressure and skin-friction lines. The contour plots indicate that the fully developed and coherent vortex structures that have been observed in the previous flight conditions (namely, primary and secondary vortices that are substantially above the inner and outer wings) are not present in this flight condition. The convergence–divergence of skin-friction lines do show the confluence of vortical layers near the midspan of the wing that likely separates and reattaches inboard near the fuselage. Separation does seem to occur, but the liftoff appears to remain close to the upper surface, either just in or just above the boundary layer. The flow does separate from the air dam and actuator pod and a small vortex seems to develop. Note, however, that no vortex is shed from the outer wing and there is no sign of a secondary vortex over the inner wing, as found in the other cases.

As shown in Fig. 8, at BL55, there is a shock wave at approximately 5% chord, due to the decelerating effect of the low sweep of the inner-wing fairing. There is another shock wave at about 30% chord on the upper surface. In the computations, there is also a shock at 20% chord of the lower-wing surface. There are, however, no measured values at this location to confirm it.

Along BL70 and BL80, several computations agree with each other, but not with the measurements. The computed results show a shock on the upper surface located well upstream of the shock shown by flight data.

The last two butt lines, BL153.5 and BL184.5, are on the outer wing, where the flow is influenced by the air dam, crank, and missile. All computational results overpredict the suction peak near the leading edge; this could be due to the leading-edge flap on the outer wing that had an upward deflection range from -5 to -9 deg, whereas the trailing-edge flap was deflected ≤ 2 deg downward in the flight test. Differences begin to grow in the computed results, especially in the aft part of the chord.

At BL153.5, the measurements might suggest a shock just before 80% chord and just before 60% chord in BL184.5. This is in disagreement with the computations that could be due to the in-flight deflected trailing-edge flap, which is not modeled in the computations. A general inspection of the butt-line C_p comparisons prompts the overall comment that the computed data agree very well among themselves, but differ substantially from the measurements, except at BL55 and BL95, where all results are in fairly good agreement.

If we accept the explanation of the negatively deflected leading-edge flap to be the cause of the discrepancies at BL153 and BL184.5, then it is the discrepancies at BL70 and BL80 that beg for explanation. The work of CAWAPI members therefore focused on carrying out several additional activities to explain the cause of this discrepancy.

C. Investigating Possible Causes of Discrepancies

The investigations are divided into two categories: one targeting possible computational reasons and the other targeting possible reasons that may have appeared during the flight test.

1. *Activities to Eliminate Possible Numerical Effects*

The activities targeting possible numerical causes were a mesh dependency study, a turbulence model effect study, a physical model study, the effect of unsteadiness, and the effect of different formulations of boundary conditions.

1) EADS [6,12] carried out a study investigating mesh dependency, particularly in and above the boundary layer. Manually adapted and solution-adapted grids were used. The finest grid solutions, both manually and solution-adapted, show a weak primary vortex over the inner part of the wing, whereas the coarser-mesh solutions show this vortex only in the most forward part of the wing. The vortical features obtained on the adapted grid are shown in Fig. 7. However, the presence of this vortex does not change the overall character of the solution [6], which may indicate that the mesh adaptation has not progressed far enough.

2) The grids that were used for all other FC calculations had the value of y^+ set by the requirement of subsonic flight, in which the Reynolds number is about half of the value of FC70. A mesh made at EADS that corrected this anomaly showed no difference in result.

3) KTH/FOI [11] and LaRC [14] carried out an investigation aimed at testing different turbulence models and their possible effect on results. No major difference was observed.

4) USAFA [15] carried out unsteady calculations using a Spalart–Allmaras model with rotational corrections (SARC)-DES. Their solution is very similar to the RANS solutions.

5) KTH/FOI [19] carried out different tests with given values of static pressure at the inlet and total states in the nozzle, as well as with mass-flow boundary conditions in the nozzle. No effect from the different boundary-condition formulations was observed.

2. *Activities to Eliminate Possible Flight Test Reasons*

The activities targeting possible flight-test reasons for the discrepancies were the effect of angle of attack and sideslip angle, the effect of change in aircraft geometry during the flight test, the effect

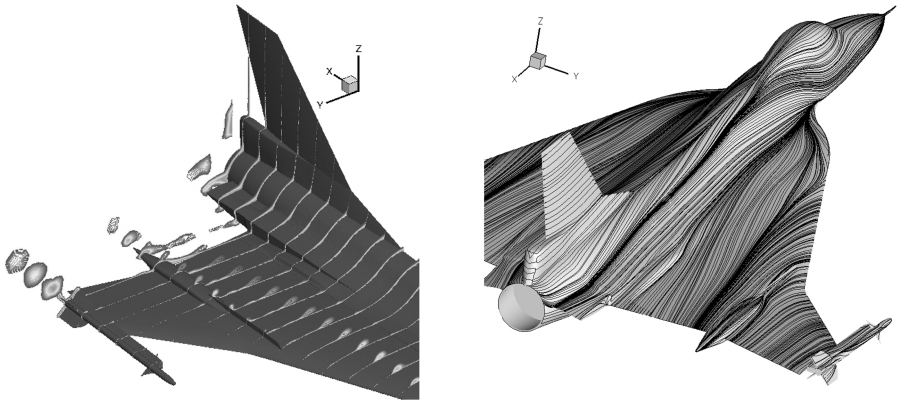

a) Sectional spanwise iso-total-pressure contours [12] b) Skin friction lines [7]

Fig. 7 Low-lying vortices over the upper surface for FC70; see Table 1 for the solutions provided by the listed organizations.

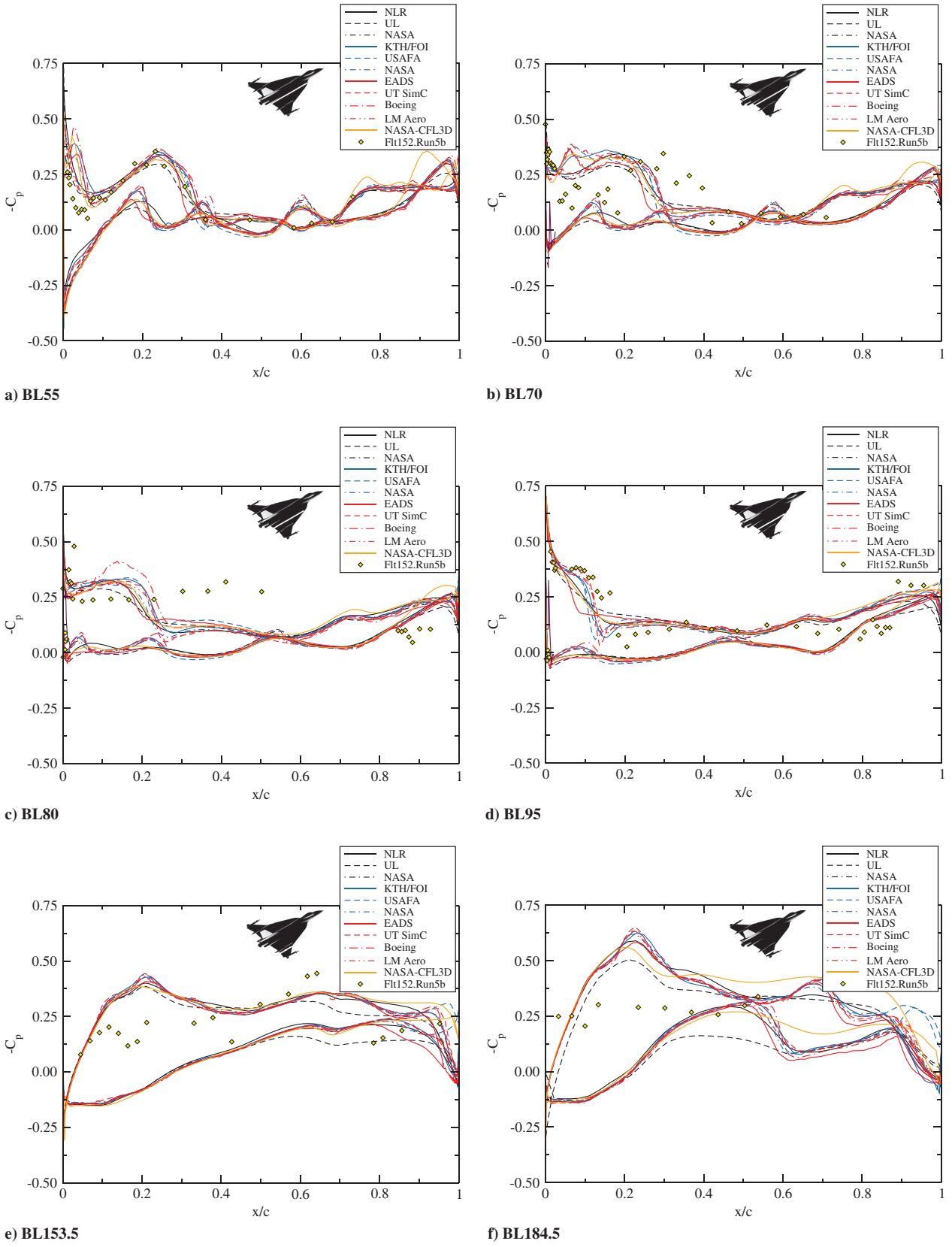

Color coding: Black - Common structured mesh
Blue - Common unstructured mesh
Red - Trimmed unstructured mesh

Fig. 8 Chordwise comparison for FC70 of pressure coefficient; see Table 1 for the solutions provided by the listed organizations.

Table 2 Computational grid sizes (pyramidal elements are included in the total volume cells counts)

Grid		Surface	Prism	Tetra	Total volume
		Triangles $\times 10^3$	Cells $\times 10^6$	Cells $\times 10^6$	Cells $\times 10^6$/nodes $\times 10^6$
RANS	Common	160	1.44	10.49	11.94/2.54
	KTH/FOI initial	158	6.12	7.40	13.56/4.36
	KTH/FOI singly adapted	433	16.81	14.65	31.52/11.03
Euler	KTH/FOI initial	158	——	8.99	8.99/1.53
	KTH/FOI triply adapted	902	——	94.71	94.71/16.20

of bending of the wing, and a check on possible corruption of flight-test data.

1) EADS and NLR carried out a study with small values of angle of attack and sideslip angle. Despite changes in the solutions, the overall characteristics of the results do not indicate that any small change of angle of attack or angle or sideslip would explain the discrepancy between CFD and flight data.

2) As pointed out in [1] post-flight-test analysis, the leading-edge flap was deployed −9 deg during the test. The University of Tennessee Simulation Center (UTSimCenter) carried out tests with a deformed mesh to investigate the possible effect of the flap deflection. The result of this analysis shows that the air dam blocked any influence of the outboard flowfield on the inboard pressure field, and thus the flap deflection does not explain the discrepancies between the computational results and the flight test.

3) The structures engineers designed the standard F-16 aircraft to sustain 9 g maneuvers, which means that the wing is stiff. At high loading, it would be significant, but at a cruise condition, the bending should be small. The computations agree well with the flight-test data at the first inboard span station (BL55) and the midspan station (BL95). If bending occurred, it would certainly also cause discrepancies in these two stations. Furthermore, the bending effect would have to be visible at the high-angle-of-attack flight conditions, which was not observed.

4) There is no indication in the flight-test reports that the flight data had been taken incorrectly or that the data has been corrupted. As a further check, KTH/FOI calculated the flowfield at FC68 and FC69 that are near transonic conditions. FC68 seems to be mostly subsonic, and the results are in good agreement with flight data. At FC69, where the supersonic portion of the flow is much larger than that for FC68 but smaller than that for FC70, the differences between computations and flight data begin to grow substantially, but they are still less than at FC70.

The last item suggests a possible cause and effect. The conditions for FC68 are $M_\infty = 0.90$ and $\alpha = 3.7$ deg, and for FC69, they are $M_\infty = 0.95$ and $\alpha = 3.6$ deg [1]. The only value that changes significantly between the three FCs is the Mach number: from 0.90 to 0.97. When there is little supersonic flow (hence, no shocks), the agreement is good, and when there is the most supersonic flow and strongest shocks, the agreement is worst. We hypothesize that the accurate simulation of a shock-wave/vortex interaction phenomena could be required to resolve the discrepancies.

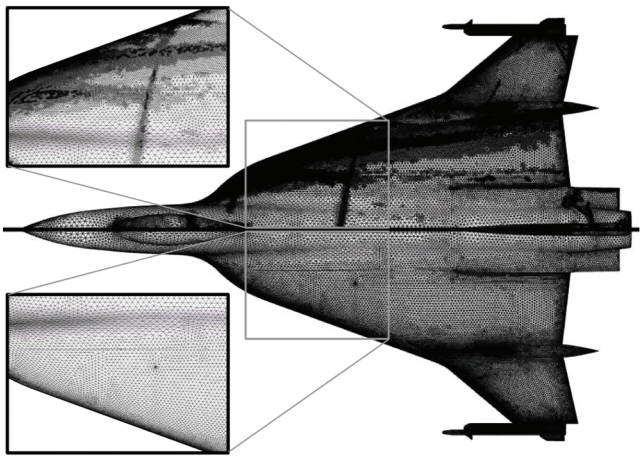

Fig. 9 Surface grids on upper surface; triply adapted mesh for Euler (top) and common RANS mesh (bottom).

D. Highly Adapted Meshes to Resolve Interaction of Vortex with Shock

The KTH/FOI team undertook an extensive study of the FC70 flowfield by generating highly adapted meshes, as shown in Table 2. KTH/FOI began with the surface triangulation of the common unstructured mesh, and after some local refinement, arrived at 158,000 surface triangles. Substantially more prism cells were added (6.12 million) in the boundary layer and fewer tetrahedral cells were included outside than in the common mesh. This became the KTH/FOI initial RANS grid. Running on this grid, the KTH/FOI unstructured code automatically adapted the mesh using a gradient sensor to produce the KTH/FOI singly adapted grid with over

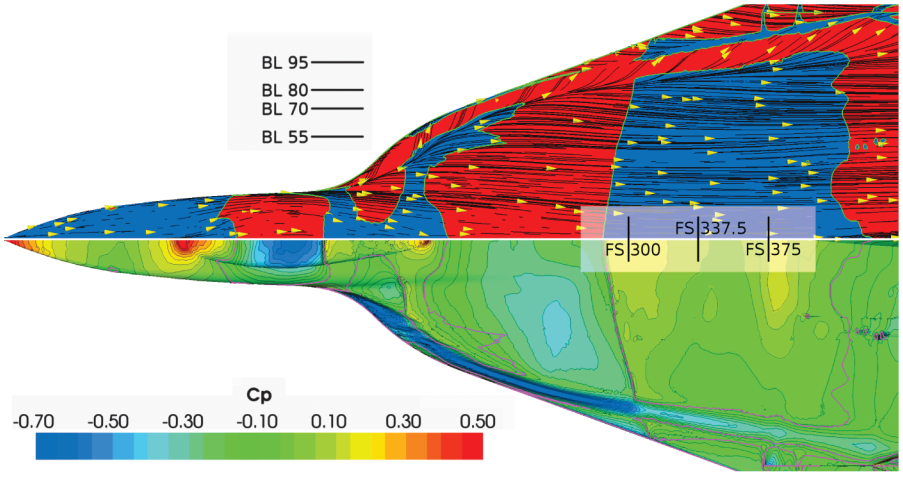

Fig. 10 KTH inviscid solution on upper surface with triply adapted mesh; streamlines superimposed over surface Mach number (top); $M < 1$ (blue), $M = 1$ (green), $M > 1$ (red); isobars of C_p [$C_p^* = -0.052$ (magenta)] (bottom).

11 million cells in total. This is more than 3 times the number in the common grid.

A second level of adaptation is not possible, because the resulting mesh would go beyond what the KTH/FOI computing facilities can handle. However, using the Euler solver, additional levels of adaptation could be handled because of the lighter computational load. Starting from the surface triangulation of the common grid, KTH/FOI created the initial Euler grid of 8.99 million nodes, and this grid was adapted 3 times. The first adaptation used the gradient sensor to mainly seek out shock waves, the second adaptation used the λ_2 sensor [20] that tracks vortex cores, and the third adaptation was again the gradient sensor. The result is the KTH/FOI triply adapted grid of 902,000 surface triangles and 16.2 million nodes.

The wing of the F-16XL is swept and sharp enough that a vortex shed from the leading edge is expected, even in an Euler simulation, although the location in which it is shed may not be correct in reality. And that is precisely what the Euler solution obtained on the triply adapted mesh indicates. Figure 9 presents the surface meshes on the upper-wing surface. The grid in the top half of the figure is the Euler mesh adapted threefold, yielding a total of 902,000 triangles on the total surface (upper and lower), and the bottom half shows the unstructured common mesh with 160,000 triangles on the total surface. The inset box is a zoom of the region in which the leading-edge vortex intersects the shock wave. The adaptation procedure picks out the major flow features, and these are clearly visible in the intensity of the triply adapted grid clustering in the Euler mesh, compared with the rather uniform grid spacing in the common mesh. The dark spanwise band is the result of two gradient-based adaptations to the shock wave. Of the three dark horizontal bands, the longest and middle one is the footprint of the primary-vortex core, as it shows three levels of adaptation: two gradient-based adaptations and, decisively, one vortex-tracking λ_2-based adaptation. This dark band results from the vortex interacting with the shock wave and persisting downstream of it. The shorter bands above and below this result from just the gradient-based adaptation. Figure 10 presents the Euler solution computed on the triply adapted grid. Streamlines superimposed over iso-Mach contours on the upper surface of the inboard wing are shown in the top half, and isobars of C_p are shown in the bottom half.

The impinging of supersonic streamlines in Fig. 10 demonstrates that a vortex is shed from the fore section of the wing leading edge upstream of the shock wave. The diverging supersonic streamlines identify the location in which the flow reattaches after the vortex liftoff. The supersonic streamlines inboard of the reattachment line decelerate to subsonic speed across the shock wave (blue region). The streamlines under the vortex, however, do not decelerate to subsonic speed, but persist through the shock wave. Outboard of the primary separation line, the supersonic streamlines again decelerate to subsonic speed across the shock. The fact that a supersonic jet of vortical flow passes through the shock (in effect, annihilating the recompression to subsonic flow, which is the usual shock-wave effect) is an important finding. Figure 10 reveals further features of this shock-wave/vortex interaction. Ahead of the shock wave, the convergence of the surface streamlines that form the liftoff of the shear layer that feeds the vortex is almost entirely supersonic flow, as is the reattachment of these streamlines. In the vortical jet downstream of the shock wave, this liftoff and subsequent reattachment occur in substantial regions of subsonic flow; that is, the supersonic streamlines reattach by decelerating to subsonic flow, presumably through a shock wave.

These features have not been seen in any of the previous RANS solutions, presumably because of insufficient grid resolution of both the shock and the vortex. A RANS solution is needed to corroborate what was found in the Euler solution. Unfortunately, the RANS solution computed on the singly adapted KTH/FOI grid shows only the suggestion that the vortex shed from the leading edge, somewhat inboard of that shed in the Euler solution, interacts with the shock wave, but has insufficient strength to penetrate through it. Therefore, we can only speculate that with still higher grid resolution, the RANS solution would proceed in the direction of the Euler solution.

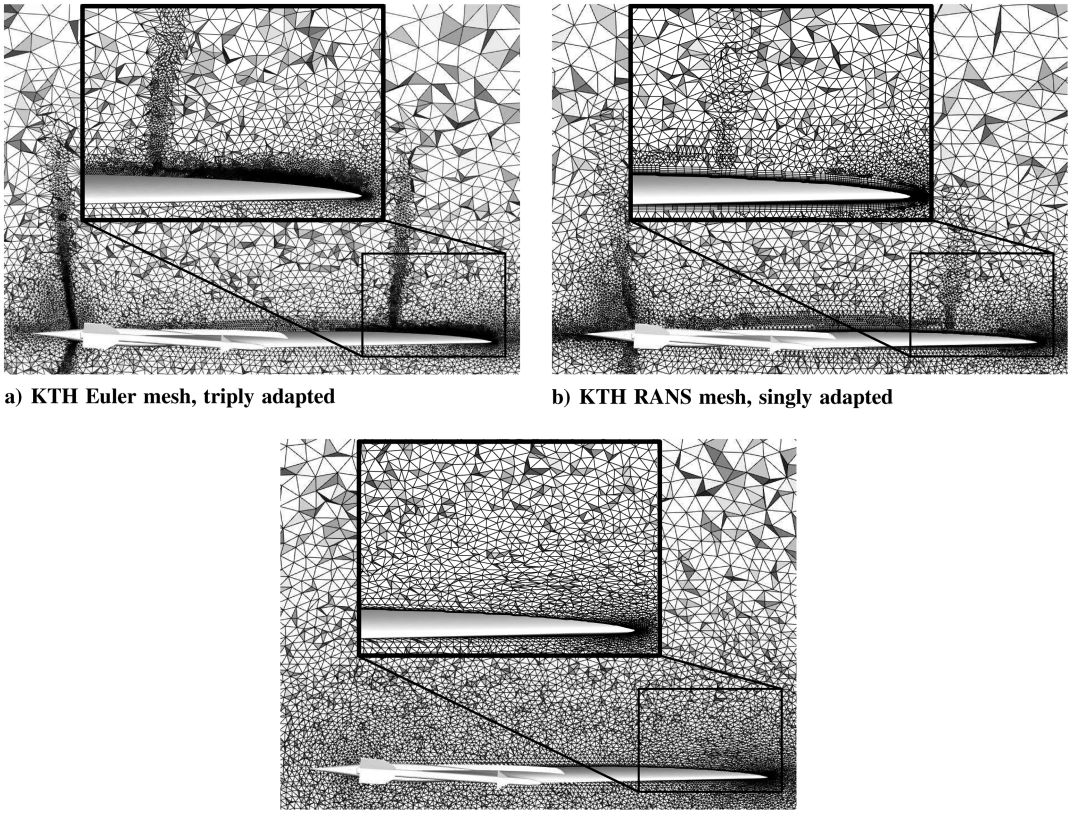

a) KTH Euler mesh, triply adapted

b) KTH RANS mesh, singly adapted

c) Common RANS mesh, no adaptation

Fig. 11 Chordwise cut through three unstructured grids in BL80 section.

E. Comparisons Along Butt-Line Sections

Figure 8 shows the largest C_p discrepancies to be at BL70 and BL80, and thus this region in the Euler and RANS solutions are of prime interest to investigate. Figure 11 presents a chordwise cut through three different unstructured grids in the BL80 section to illustrate the effects of mesh adaptation. The inset frame is a magnification of the first third of the wing chord that contains the region of the shock–vortex interaction. The dark bands of clustered cells in Figs. 11a and 11b visualize the location of the shock in section BL80 and the density of cells over the upper surface, which are features not seen in Fig. 11c of the common grid. Figure 12 compares the values of C_p computed on the triply adapted Euler grid, the singly adapted RANS grid, and the common RANS grid with the values measured in the flight test for FC70.

In BL55, all three computed values agree reasonably well with each other and with the flight-test results, although at the first 10% of the chord, the computed results overpredict the suction there. In the BL95 section, the two RANS results agree with each other and with the measured data. The Euler results, however, differ from these. The flow does not compress through the shock to the subsonic values at about 15% chord as it does for the RANS result and the measurements. Instead, it expands further out to about 20% chord and then gradually compresses (isentropically) to about 40% chord; that is, there is no evidence that a shock is transversed. The following explanation is offered for this.

If BL95 were to be marked in Fig. 10, it would pass through the region of interaction between the vortex and the shock wave. The footprint of the vortex is supersonic (hence, no compression), which only comes further downstream when section BL95 passes outside of the vortex footprint. We can also conclude then that the position of the vortex in the Euler solution is not realistic.

At BL80, the two RANS result again agree with each other and indicate the shock just past the 20% chord location. The Euler result displays a substantial suction peak at the nose and then a very sharp shock just past 20% chord that confirms the RANS computation, but all three results are in contradiction to the measurements that indicate supercritical flow to at least 50% and maybe further. What is found at BL95 and BL80 then suggests the following explanation. If we could compute RANS with sufficient resolution, the vortex footprint would remain supersonic through the shock, as we see in the Euler solution, but it would lie inboard of the location of the Euler result.

We see in BL95 how the C_p values remained supercritical across the shock wave, but in RANS, this would occur at approximately BL80. If this suggestion holds true, then the flight tests would confirm the passing of the supercritical vortex through the shock wave.

In BL70, the two RANS values agree closely, and the sharp shock in the Euler results is in reasonable agreement with RANS, but the measurements show no evidence of the shock. The measurements rather show a continuous rise and fall in C_p reminiscent of the Euler-computed values at BL95; in other words, the BL70 line could also be cutting across the vortex footprint near the shock–vortex interaction zone.

F. Comparisons Along Fuselage Stations

Let us further investigate the nature of the shock–vortex interaction and, especially, the character of the flow downstream of the shock wave. For this purpose, it is useful to look in spanwise sections at the constant chord position. Figure 13 shows the spanwise cut through the three different unstructured grids in the FS337.5 section to illustrate the effects of mesh adaptation on the vortex core just behind the shock wave. The upper inset frames of Figs. 13a and 13b present a magnification of the outer half of the cross section. The lower inset frames present the same area as for the upper

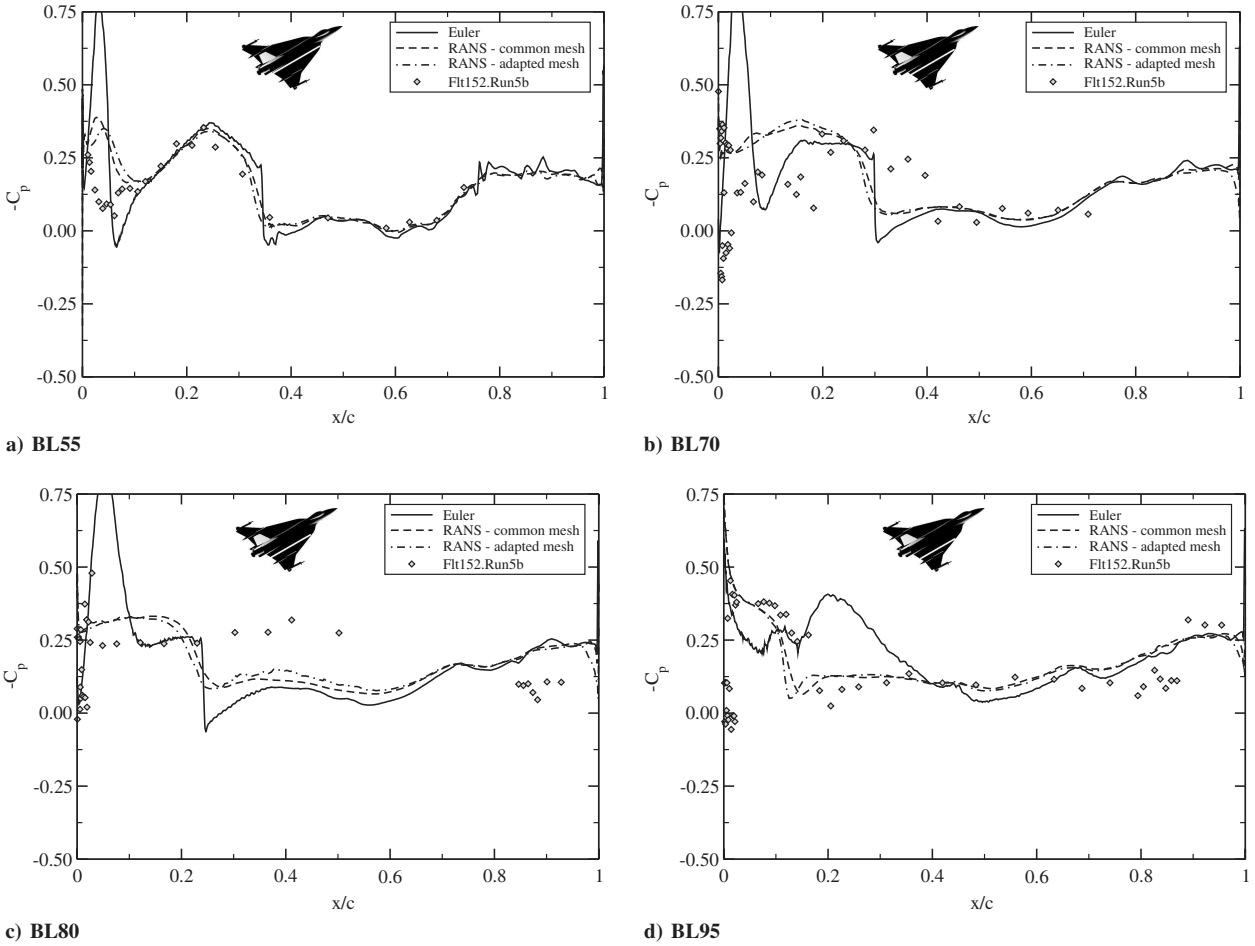

a) BL55 b) BL70

c) BL80 d) BL95

Fig. 12 Chordwise comparison of computed and measured surface C_p for FC70.

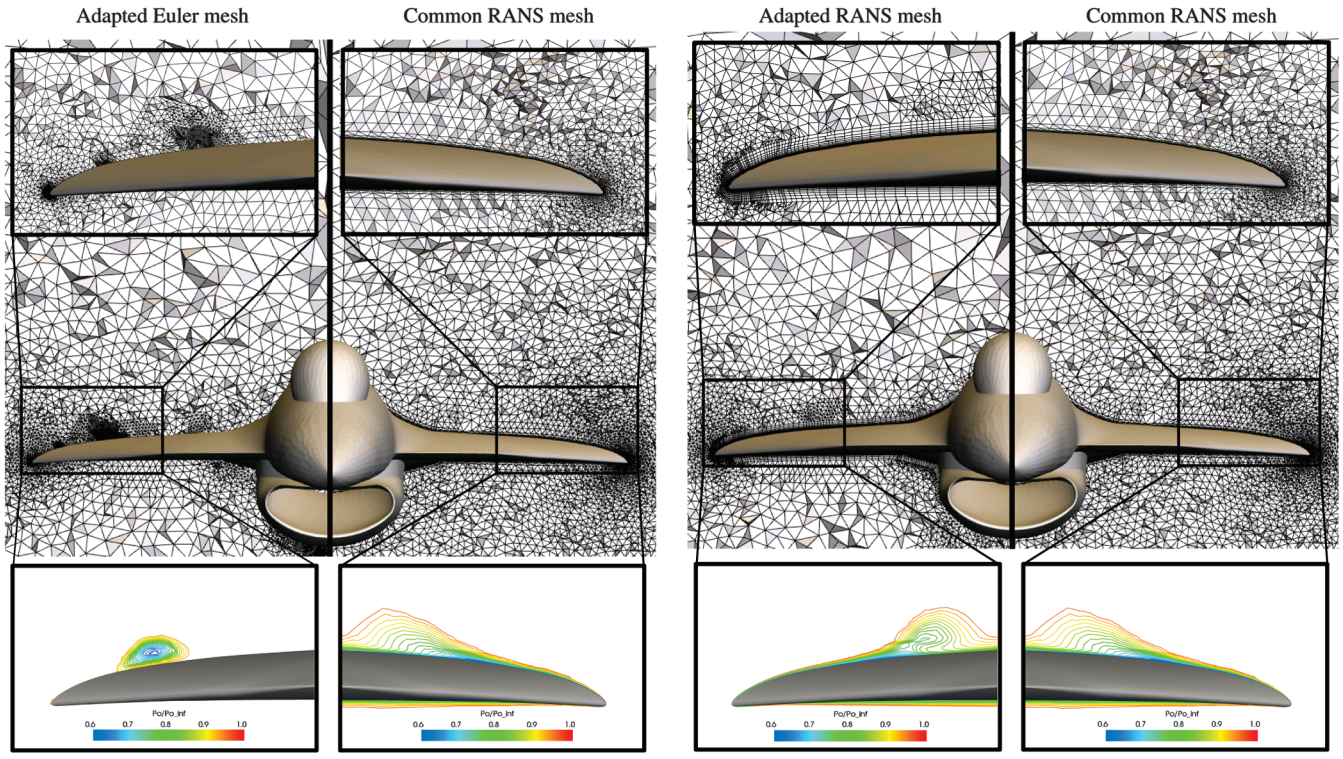

a) Left: triply adapted Euler grid; right: common RANS mesh

b) Left: singly adapted RANS grid; right: common RANS mesh

Fig. 13 Spanwise cuts at FS337.5 for three different unstructured solutions; magnified mesh and total-pressure-loss isolines.

magnification inset, but the total-pressure-loss isolines are plotted for the respective cases.

The left half of Fig. 13a presents the Euler mesh with three levels of adaptation, and the right half presents the common unstructured mesh for RANS with no adaptation. The left half of Fig. 13b presents the RANS mesh with one level of adaptation, and the right half presents the common unstructured mesh for RANS with no adaptation. The large dark region of clustered cells in the center of the left inset frame of Fig. 13a is the grid adaptation to the vortex core and gradients in the Euler solution; these gradients indicate the relative location of the vortex core along the span and above the wing. In comparison with the left inset, it also indicates the increased grid

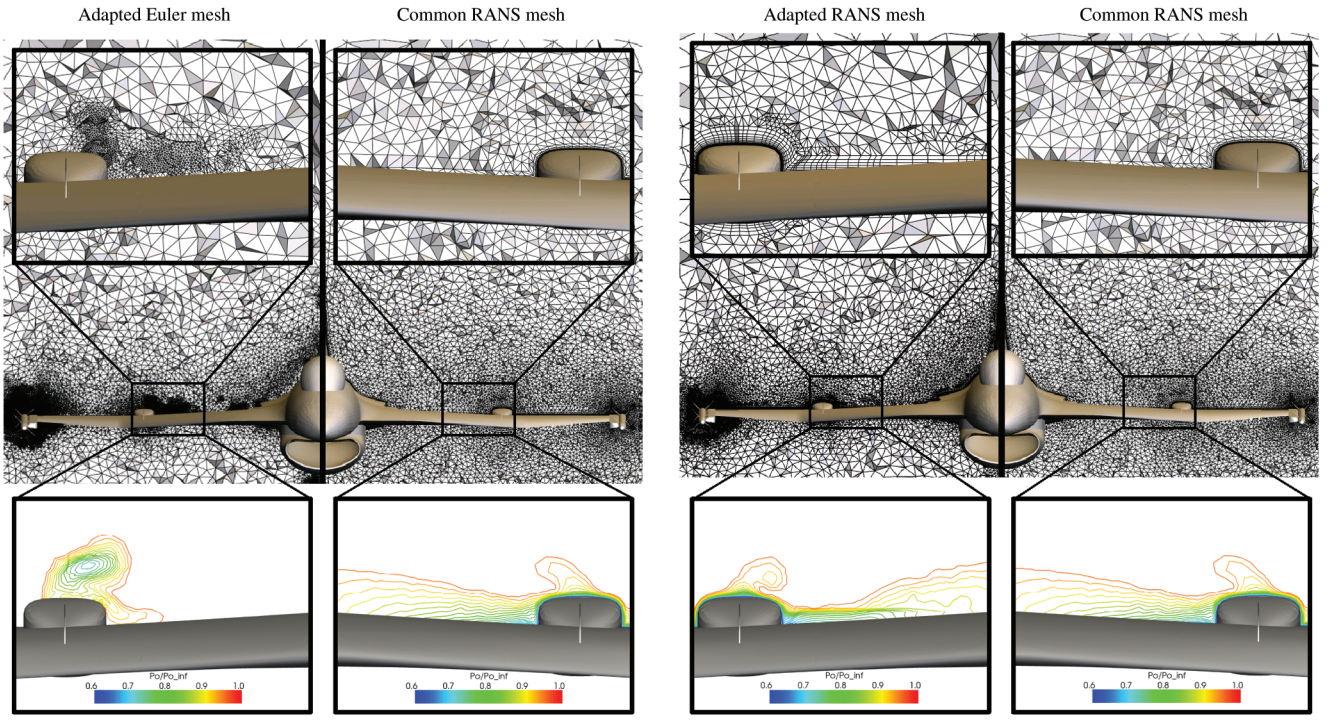

a) Left: triply adapted Euler grid; right: common RANS mesh

b) Left: singly adapted RANS grid; right: common RANS mesh

Fig. 14 Spanwise cuts at FS492.5 for three different unstructured solutions; magnified mesh and total-pressure-loss isolines.

resolution relative to the common grid. Compare this with the less dark region of clustered cells along the right edge of the left inset frame of Fig. 13b, which is the corresponding grid adaptation to the vortex core in the singly adapted RANS solution, less than that for triply adapted Euler grid, but more than that for the common grid. The total-pressure-loss isolines reveal the same picture as the analysis of the adapted-mesh regions.

The compact circular isolines of the Euler solution in Fig. 13a reveal the location of the compact vortex. The superior resolution of the vortex in the Euler case is clear when comparing the isolines of total-pressure-loss to the common solution. By analyzing Fig. 13b, it is possible to discern the effect of mesh adaptation on the resolution of the vortex for the RANS cases. The location of the vortex of the RANS cases does not change substantially, but the adapted RANS solution shows an improved vortex resolution with a discernible vortex core. This clearly indicates that the vortex core in the Euler solution is about the same distance above the wing, but about 15% span further outboard than the vortex core in the singly adapted RANS solution. This finding supports our argument in the previous section that claimed that the features seen in the Euler-computed C_p values in BL95 are comparable with the flight-test values in BL80.

In an exactly analogous manner, Fig. 14 shows the spanwise cut through the three different unstructured grids in the FS492.5 section to illustrate the effects of mesh adaptation to the vortex core just before the trailing edge of the wing. Now there are two dark regions of clustered cells in zoom frame of the Euler grid (left side of Fig. 14a). The inboard adaptation is a result of the very weak leading-edge vortex, and the outboard region is due to the vortex shed from the air dam. Although the cell density is lower, due to the lower degree of adaptation, two regions in the zoom frame of the RANS grid (left side of Fig. 14b) have the identical interpretation, which is in fact consistent with the visualization of the two vortices at the trailing edge in Fig. 7a. The total-pressure-loss isolines at the FS492.5 section reveal the location of either one or two vortices. The location of the air-dam-induced vortex is fixed for all three cases. In the RANS solutions, this vortex is located above the actuator pod, whereas the main-wing leading-edge vortex is recognizable further inboard.

For the RANS solutions, the further-inboard-located leading-edge vortex is so weak at this station that the total-pressure-loss isolines show no clear evidence of its location. In the Euler solution, the further-outboard-located leading-edge vortex merges with the air-dam vortex. This results in a markedly stronger and wider vortex above the actuator pod. Figure 15 compares the values of C_p computed on the triply adapted Euler grid, the singly adapted RANS grid, and the common RANS grid with the values measured in the flight test for FC70 in the sections FS300, FS337.5, FS375, and FS492.5. At FS300, which is just in front of the shock, the Euler-computed values show a suction peak at approximately 85% span. If we would place this at about 70% span to account for the vortex in the Euler solution being 15% further outboard, then this peak would be in fair agreement with the suction peak in the flight-test data at about 70% span.

Note also that there is a small peak in the singly adapted RANS-grid solution at about this same position, which, with further adaptation, might increase the level of the predicted values. Station FS337.5 is downstream of the shock wave, and the three measured

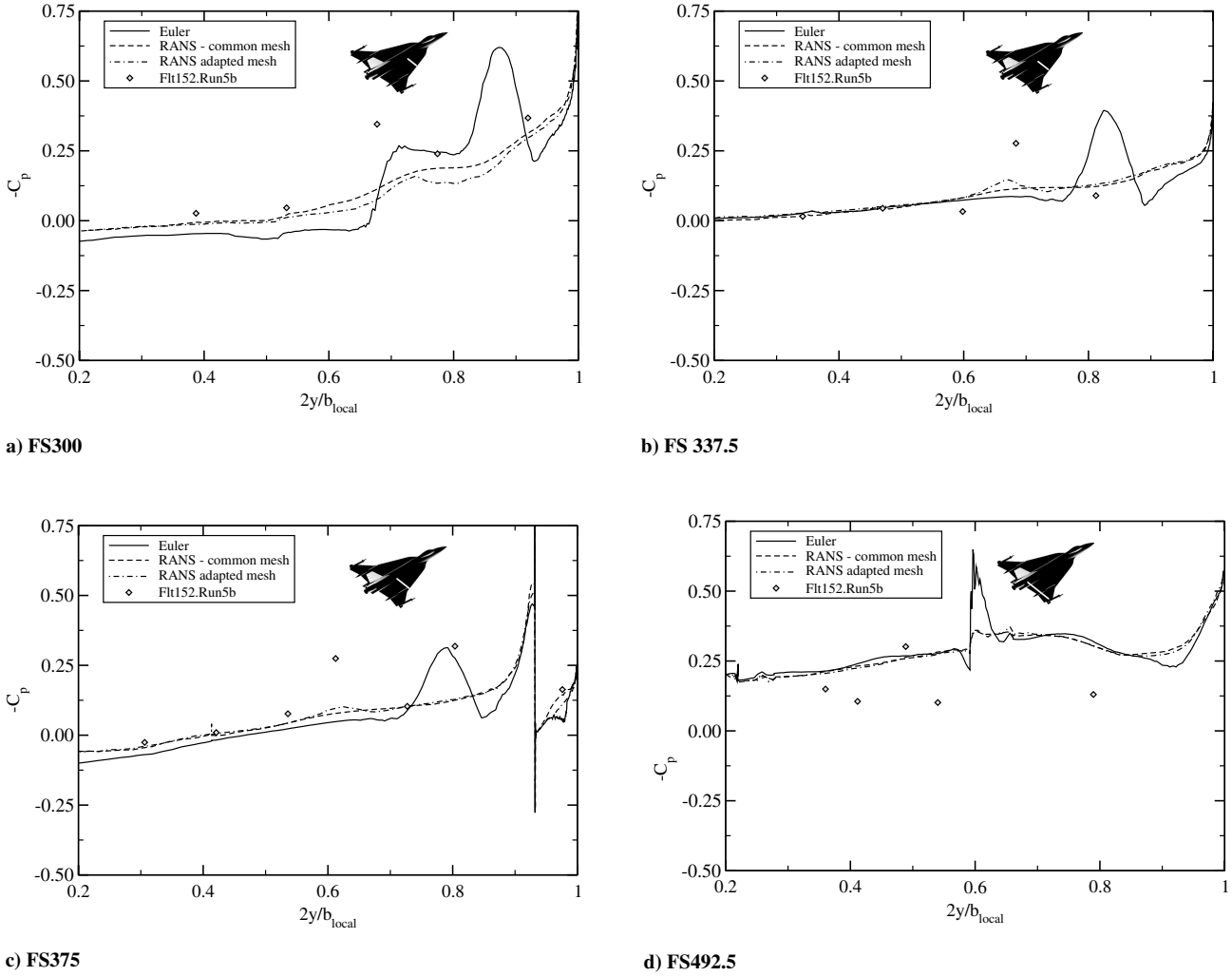

a) FS300

b) FS 337.5

c) FS375

d) FS492.5

Fig. 15 Spanwise comparison of computed and measured upper surface C_p for FC70.

data values clearly indicate a supercritical suction peak. The Euler solution presents a peak, again about 15% further outboard, and the singly adapted RANS result shows the emergence of a small peak in the position that agrees with the measured one. Station FS375 is at the beginning of the air dam, and the flight data seem to suggest two suction peaks. The inboard peak at about 60% span is the leading-edge vortex suction, consistent with the smaller, singly adapted, RANS peak and the outboard peak in the Euler result. The second peak in the data measured at 80% span is due to the vortex shed from the air dam, consistent with the two vortices seen in Fig. 7a. Finally, the flight-test data in section FS492.5 are too sparse to distinguish the two vortices, but the few points that exist are consistent with such an interpretation.

G. FC70 Concluding Remarks and Lessons Learned

Flight condition 70 is the highest-Mach-number case examined by all participating organizations, as well as the highest-Reynolds-number case and the lowest-angle-of-attack case, and so, in a sense, it is an extreme of the examined flow conditions. It is the only case examined with interacting supercritical vortex flow and shock waves. Before the CAWAPI team started work on FC70, the major focus was to determine the best practices needed to accurately simulate the vortical-flow features and pressure distribution over the aircraft. The geometry used and the mesh generated was the same for all cases, including the transonic one. Use of all of the grids that lead to reasonable results for all of the other test flights did not produce satisfactory results for this flight condition. It took a detailed Euler simulation with a highly adapted mesh to reveal the occurrence of a shock–vortex interaction that significantly changed the surface pressure distribution. One conclusion is that if the mesh used offers sufficient resolution to resolve the shock–vortex interaction problem, then one observes a jet of supersonic vortex flow blowing through the shock wave, delaying recompression to further downstream than with no grid refinement. If the goal is to resolve the detailed pressure distribution over the aircraft, then this feature must be resolved.

The lessons learned are as follows:

1) At a high Mach number, high Reynolds number, and low α, expect shock–vortex interaction. This is difficult to resolve because the vortex does not lift very far off the surface and out above the boundary layer.

2) The dimensionless sublayer-scale distance y^+ on the surface is not a conclusive indicator that one has a sufficient mesh. The mesh must resolve the vortex liftoff and interaction across the entire boundary layer and beyond.

3) Adapt the mesh for both shock and vortex. The occurrence of the supercritical vortex core that persists across the shock wave requires resolving both the shock and the vortex. Adapting to just one of these will miss this combined effect. For example, the grids that were sufficient for all of the other flight conditions (i.e., those that had just vortex phenomena) missed the shock–vortex interaction in FC70. It could take well more than an order-of-magnitude increase in grid cells to resolve the associated interaction region and boundary layer.

4) Shock–vortex interaction may be unsteady. This phenomena presumably has some unsteady components to it, but this aspect was not investigated here. We expect that these aspects would occur on a scale that would require high grid resolution of the interaction region to be captured. There is no reason to expect that the difficulties (and features) encountered with FC70 are in any way specific to the F-16XL airframe. We are convinced that the same type of shock–vortex interaction will occur on other similar types of military aircraft at similar (routine) flight conditions.

V. Perspectives

A. Computation Progress Since CAWAP

The Lamar et al. [1] flight and wind-tunnel test data are presented and compared with CFD predictions. The code CFL3D was used, which was developed at LaRC and is widely used in the United States. A patched multiblock grid was generated on a simplified half-configuration of the F-16XL, with the intention to focus grid points on the wing to resolve vortices. The wing-tip missile and launcher were modeled, as was the air dam, but the vertical fin was not included. The final grid had 1.37 million cells, with the first cell spacing set for the wind-tunnel Reynolds number. The flight Reynolds number was computed using a wall function. The turbulence model used was Baldwin–Lomax with the Degani–Schiff modification for vortical flow. The calculations were run on the Cray C-90, and each steady calculation required around 24 h. The convergence was stopped after the residual had been driven down 2–3 orders, which is unlikely to be sufficient. Finally, the commercial package Fieldview was used to visualize the vortices.

For the vortical-flight conditions considered in CAWAPI, the C_p distributions generally show better agreement inboard. However, suction peaks are underpredicted. One contribution to this is the coarseness of the grid. There were also significant discrepancies between the skin-friction and boundary-layer predictions and measurements. For FC70 (transonic case), good agreement was again obtained inboard, with very poor comparison with flight measurements outboard of the crank. A possible cause of this was suggested to be the uncertain deployment of the leading-edge flaps and the ailerons. It was also stated that the convergence of the transonic case was more difficult.

The computing power available to the participants in CAWAPI was 1–3 orders of magnitude larger than that available for the [1] calculations. The codes used in AVT-113 all ran on distributed memory parallelism, with the exception of the NLR code, which exploits a very high vector performance. The cost of computing has fallen to such an extent that many participants used local resources, whereas Lamar et al. [1] relied on an allocation on a supercomputer.

Emphasis in the working group was placed on retaining as much of the detailed definition of the aircraft as possible. A number of minor simplifications were made [3], and to a very large degree, the goal was achieved. A number of partners were able to use their own grid-generation tools to generate a grid around the extremely complex shape. It seems likely that the geometry simplifications by Lamar et al. [1] were driven by the need to keep the number of grid points down.

Several CAWAPI partners used their own tools to generate grids around the complex F-16XL shape. The most direct comparison with Lamar et al. [1] is with the structured-grid generation of NLR. It is clear that the tools developed at NLR represent a major advance from what was available at the time of Lamar et al. [1]. A significant development is the ability to generate unstructured grids for viscous flows through the exploitation of grown layers in the boundary layer. A number of codes were able to generate grids in a reasonable time. Finally, EADS-MAS and KTH/FOI made effective use of automatic grid adaption, the use of which is not currently as widespread as might have been expected.

All participants in CAWAPI used turbulence treatments based on partial differential equations, in contrast to the algebraic model used by Lamar et al. [1]. The simplest turbulence treatment used was one- or two-equation turbulence models. Rotation corrections to Boussinesq-based models seemed to allow good solutions without too much difficulty, to the extent that they could be described as routine. Some partners used Reynolds stress models, but without significant obvious benefit. Finally, some partners used DES.

Some partners showed that it is now possible to resolve unsteady effects, showing significant unsteadiness downstream of the crank. The origins of this need further study, but could originate from an interaction of the inner- and outer-wing vortices or an interaction between the inner-wing vortex and the air dam.

Discretization and solution schemes have advanced little since Lamar et al. [1]. The efficiency of the schemes was not really considered in CAWAPI, but interesting information about the performance on grids required for such a complex geometry could be obtained in the future. The spatial accuracy of the codes has not improved noticeably since the time of Lamar et al. [1].

Possibly driven by improved computing, the visualization of solutions produced in CAWAPI far exceeded that shown in [1]. Visualization through isosurfaces and surface streamlines and the

automatic detection of vortex cores all effectively showed the behavior of the solutions, including unsteady effects.

B. Technology Readiness Level Improvements

The following statements were made by industry team members of CAWAPI regarding the benefits accrued by their participating organizations in CAWAPI. Obviously, it is this group that will be the end users of any new technology developed, and in that role, the concept of TRL improvement is not only academic, but economic, because company growth or survival can be an outcome. (The statements are arranged in the order received.)

Willy Fritz of EADS-MAS comments,

> Within the CAWAPI, EADS made essential experience with the solution-based grid adaptation at complex configurations. We saw the benefit of the solution-based grid adaptation, but we also learned that it is sometimes a laborious task. For the future application of the grid adaptation, we got very useful guidelines. Our daily business is not only to calculate force and moment coefficients or pressure distributions, but also to find the physical causes for unexpected effects that were observed during the flight test. Therefore, we need a realistic computational model with correct slat, flap, and rudder settings. So we have to use hybrid grids.
>
> These unexpected effects occur at the high-angle-of-attack range or at special maneuvers. For these flow conditions, a carefully generated grid is an essential key toward a realistic numerical outcome. As grid-independent RANS solutions with globally refined hybrid grids are never possible in our production environment, the only possibility to minimize the grid dependency of the numerical outcome is again the use of solution-adapted grids. Especially at vortical-flow structures at high angles of attack, even small vortices coming from slat corners, strakelets, etc., can become very important, as they can trigger or delay vortex breakdown at the big primary vortices. Even in apparent very fine grids, such small vortices are represented too weakly. The solution-based grid adaptation very often tracks such small vortices and we get considerable improvements of the numerical outcome.
>
> Since the CAWAPI, we know that the solution-based grid adaptation at such complex configurations can be handled and we know how to handle it. By this, the experience of CAWAPI has improved the readiness level of the application of our CFD tools. (Without this experience we never would have tried a solution-based grid adaptation at a complex configuration.) CAWAPI was also the first possibility to validate our CFD tools on a full-scale fighter-type aircraft with flight-test pressure distributions. (Agreements of the force and moment coefficients can be accidental, as disagreements in the pressure distributions can cancel out each other.)

Bruce Davis of Lockheed Martin Aeronautics Company comments,

> Lockheed Martin Aeronautics Company (LM Aero) as a designer, developer, and manufacturer of advanced military aircraft is keenly aware of the importance of accurate CFD simulations. CFD is used in a variety of ways, from improving aerodynamic design to providing aerodynamic loads to improving the separation of stores from aircraft. The validation of CFD codes is of central importance, because this increases the confidence in CFD results and can potentially save costly wind-tunnel and flight-test time.
>
> LM Aero has recently been involved in updating Falcon, its general-purpose Navier–Stokes flow solver. This effort, and specifically the validation of the flow solver, has coincided with the involvement in the CAWAPI program. This timely involvement has provided LM Aero with a challenging validation suite with high-quality flight-test data. If for no other reason, the availability of this validation case has made the participation in CAWAPI a valuable experience for LM Aero, and the validation of our flow codes against this test database will not end with the CAWAPI program.
>
> LM Aero did not generate the computational grids for this problem, but rather used grids supplied by the UTSimC. The grid used did not fully resolve the viscous sublayer of the turbulent boundary layer, but rather used wall functions. The LM Aero simulations consistently underpredicted the suction peaks lying under the main vortices. The suspicion is that the use of wall functions for this particular problem is not appropriate and that simulations with the fully resolved viscous sublayer will bear this out. Even with the use of wall functions, the half-symmetry grid contained 42 million cells, which is the largest grid used to date for a Falcon V4 simulation. In this sense, it allowed LM Aero to evaluate the code, as well as various utilities, for very large problems.

Todd Michal of Boeing-Phantom Works comments,

> Participation in the CAWAPI program has provided many tangible and intangible benefits to Boeing. The CAWAPI collaboration has provided an opportunity to establish contacts with leading researchers while working toward the common goal of expanding the envelope of CFD analysis. Perhaps the most beneficial aspect of this program has been the establishment of best practices for CFD analysis for complex high-angle-of-attack vortex-dominated flowfields. Through our involvement, guidelines for grid properties, turbulence model, and algorithm option selection have been established that will directly benefit future Boeing programs.
>
> Another benefit of the CAWAPI effort has been the chance to compare and validate Boeing tools and processes with other industry, university, and government codes. The comprehensive set of flight-test results available for this effort enabled CFD to be validated in new parts of the flight envelope. This validation highlighted several areas in which CFD tools do very well and, perhaps equally important, areas in which current CFD methods fall short. It is our belief that identification of these shortcomings will guide future research efforts that will benefit Boeing as well as the greater CFD community.
>
> In addition to benchmarking our current CFD capability, the CAWAPI program provided an excellent opportunity to investigate the use of new technologies to help solve complex problems. Capabilities such as grid adaptation, new turbulence models, and new numerical algorithms were all investigated. These studies provided a great deal of information that will help with the development and deployment of these new technologies.

VI. Conclusions

Although differences were observed in the comparison of results from 10 different CFD solvers with measurements, these solvers all functioned robustly on an actual aircraft at flight conditions, with sufficient agreement among them to conclude that the overall objectives of the CAWAPI endeavor have been achieved. In particular, the status of CFD as a tool for understanding flight-test observations has been confirmed. A number of specific points have arisen from CAWAPI:

1) The state-of-the-art computations for FC70 showed a remarkable degree of agreement. However, the agreement with measurements was not close. After the assessment of several possible explanations, it is suggested that this discrepancy is due to the poor prediction of a concentrated leading-edge vortex and its interaction with a shock. This conclusion would not have been reached without performing a high-resolution inviscid analysis. These computations were only performed after the discrepancies between the state-of-the-art tools and measured data could not be explained. If this were an a priori computational campaign, the conventional computations showing such a consistent agreement with each other would have been interpreted differently; then only a later flight-test campaign would have recognized the discrepancy. This stands in clear contrast to the computations at FC25, for which, due to the statistical tools, the discrepancy between various computations would have triggered an alert. The state-of-the-art computations for FC70 would not have triggered such an alert. As shown at this condition, a necessary advance of the CFD tools is the reduction of discretization error, either from massive feature-driven grid adaption or higher-order schemes.

2) Time-accurate simulations of the high-angle-of-attack flight condition FC25 showed significant unsteadiness arising from the interactions of vortices downstream of the crank. This was unanticipated at the outset of the working group from a consideration

of the flight-test data. In this respect, the CFD solutions have stimulated a reinterpretation of the measurements.

3) Two considerations caused concern about the grid convergence of the CFD solutions. First, there is a large spread of the solutions for properties such as vortex strength, as indicated by suction footprints on the wing surface. Second, grid-adaption studies by some partners showed significant improvements in, for example, resolving secondary vortices. Given the large grids used (10–20 million points for half-bodies), this emphasizes that advances in adaption and discretization-scheme accuracy are important.

4) The evaluation of predictions of boundary-layer profiles showed the advantages of DDES over DES in this region.

5) The generation of a block-structured grid in a similar time frame to that required by an unstructured grid showed what can be achieved with advanced grid-generation tools generated by one of the CAWAPI partners.

The work of Lamar et al. [1] provides a suitable benchmark for identifying the advances since 2001. This reference described an application of CFD to the F-16XL using the state-of-the-art tools at the time. The ability of the current working group to use grids of much higher resolution has brought the predictions more in line with measurements. In addition, advances in block-structured grid-generation tools have allowed the retention of almost all of the geometrical features in structured grids. Turbulence treatments that overcome the limitations of the Boussinesq assumption for vortical flow were used routinely. Unsteady effects were simulated by some partners and were shown to be significant. The accuracy of the spatial discretization has not advanced since 2001, and this has been shown to be significant. To balance this, some advances have been shown in grid adaption for unstructured codes.

Appendix A: Force/Moments

This Appendix shows the force/moments data: lift C_L, drag C_D, friction drag C_{D_f}, and pitching moment C_M for several CFD solutions, along with the statistical analysis for each flight-tested flight condition (see Tables A1–A12). For sideslip flight conditions FC50 and FC51, the comparisons include the component values of

Table A1 Flight condition FC25 force/moment coefficients[a]

Coefficient	NLR	KTH/FOI	USAFA	LaRC unstructured	EADS[b]	UTSimC	Boeing
C_L	0.77328	0.79789	0.78402	0.80199	0.82795	0.76553	0.75560
C_D	0.45088	0.44800	0.40537	0.49923	0.44577	0.59244	0.52836
C_{D_f}	0.01270	0.01060	——	0.01989	——	0.01373	0.01030
C_M	0.02525	0.01061	0.01645	0.01653	−0.00492	0.00707	0.02228

[a]See Table 1 for the solutions provided by the listed organizations.
[b]Data without inlet and nozzle surface

Table A2 Flight condition FC25 force/moment coefficients: statistical analysis[a]

Coefficient	$\hat{\mu}$	$k\hat{\sigma}$	No. of identical solutions	No. of outliers
C_L	0.78402	0.04307	6	1
C_D	0.45088	0.12346	6	1
C_{D_f}	0.01270	0.00687	4	1
C_M	0.01645	0.01858	6	1

[a]See Table 1 for the solutions provided by the listed organizations.

Table A3 Flight condition FC19 force/moment coefficients[a]

Coefficient	NLR	KTH/FOI	USAFA	LaRC unstructured	EADS [b]	UTSimC	LM Aero
C_L	0.43846	0.44693	0.37006	0.43851	0.46798	0.44190	0.44590
C_D	0.13289	0.13469	0.11084	0.15788	0.13648	0.16158	0.14265
C_{D_f}	0.00932	0.00772	——	0.01531	——	0.00919	——
C_M	0.00699	0.00124	0.00124	0.00112	−0.00590	−0.00021	−0.00390

[a]See Table 1 for the solutions provided by the listed organizations.
[b]Data without inlet and nozzle surface.

Table A4 Flight condition FC19 force/moment coefficients: statistical analysis[a]

Coefficient	$\hat{\mu}$	$k\hat{\sigma}$	No. of identical solutions	No. of outliers
C_L	0.44190	0.05434	6	1
C_D	0.13648	0.03000	7	0
C_{D_f}	0.00926	0.00625	4	0
C_M	0.00112	0.00744	7	0

[a]See Table 1 for the solutions provided by the listed organizations.

Table A5 Flight condition FC7 force/moment coefficients[a]

Coefficient	NLR	KTH/FOI	USAFA	LaRC unstructured	EADS[b]	UTSimC	Boeing	LM Aero
C_L	0.43560	0.44258	0.43868	0.44076	0.45993	0.43996	0.44510	0.44430
C_D	0.13932	0.14571	0.13019	0.16942	0.08909	0.19609	0.14131	0.15135
C_{D_f}	0.01029	0.00850	——	0.01708	——	0.01104	0.00840	——
C_M	0.00772	0.00236	0.00300	0.00206	−0.00475	−0.00154	−0.00191	−0.00345

[a]See Table 1 for the solutions provided by the listed organizations.
[b]Data without inlet and nozzle surface

Table A6 Flight condition FC7 force/moment coefficients: statistical analysis[a]

Coefficient	$\hat{\mu}$	$k\hat{\sigma}$	No. of identical solutions	No. of outliers
C_L	0.44036	0.01391	7	1
C_D	0.14351	0.05344	7	1
C_{D_f}	0.01029	0.00566	5	0
C_M	0.00026	0.00710	7	0

[a]See Table 1 for the solutions provided by the listed organizations.

Table A7 Flight condition FC50 force/moment coefficients[a,b]

Coefficient	NLR	KTH/FOI	USAFA	LaRC unstructured	UTSimC
C_L	0.52908	0.53241	0.53569	0.52395	0.53485
C_D	0.15481	0.18115	0.12656	0.20383	0.18526
C_{D_f}	0.00907	0.00998	——	0.01447	0.00921
C_Y	−0.03941	——	−0.05068	——	——
C_M	0.00095	−0.00844	−0.00414	−0.00045	−0.0051
C_X	−0.02240	−0.01092	−0.01855	−0.01771	——
C_Z	0.01706	0.01450	0.01200	0.01167	——

[a]See Table 1 for the solutions provided by the listed organizations.
[b]$\beta = 5.31$ deg.

Table A8 Flight condition FC50 force/moment coefficients: statistical analysis[a,b]

Coefficient	$\tilde{\mu}$	$k\hat{\sigma}$	No. of identical solutions	No. of outliers
C_L	0.53241	0.00863	5	0
C_D	0.18115	0.05616	5	0
C_{D_f}	0.0096	0.00493	4	0
C_Y				
C_M	−0.00414	0.00664	5	0
C_X	−0.01813	0.00840	4	0
C_Z	0.01325	0.00449	4	0

[a]See Table 1 for the solutions provided by the listed organizations.
[b]$\beta = 5.31$ deg.

Table A9 Flight condition FC51 force/moment coefficients[a,b]

Coefficient	NLR	KTH/FOI	USAFA	LaRC unstructured	UTSimC
C_L	0.49612	0.51564	0.50485	0.49180	0.48839
C_D	0.14019	0.16695	0.11232	0.18600	0.21902
C_{D_f}	0.00903	0.00967	——	0.01426	0.01035
C_Y	0.03508	——	0.04237	——	——
C_M	0.00155	−0.00817	−0.00485	−0.00068	−0.0027
C_X	0.01820	0.01058	0.01558	0.01436	——
C_Z	−0.01537	−0.01405	−0.00990	−0.00989	——

[a]See Table 1 for the solutions provided by the listed organizations.
[b]$\beta = -4.58$ deg

Table A10 Flight condition FC51 force/moment coefficients: statistical analysis[a,b]

Coefficient	$\tilde{\mu}$	$k\hat{\sigma}$	No. of identical solutions	No. of outliers
C_L	0.49612	0.02004	5	0
C_D	0.16695	0.07128	5	0
C_{D_f}	0.01001	0.00439	4	0
C_Y				
C_M	−0.00270	0.00652	5	0
C_X	0.01497	0.00552	4	0
C_Z	−0.01198	0.00495	4	0

[a]See Table 1 for the solutions provided by the listed organizations.
[b]$\beta = -4.58$ deg

Table A11 Flight condition FC70 force/moment coefficients[a]

Coefficient	NLR	KTH/FOI	USAFA	LaRC unstructured	EADS[b]	UTSimC	LM Aero
C_L	0.11682	0.12276	0.12044	0.12080	0.12641	0.12510	0.12412
C_D	0.04077	0.03901	0.04193	0.05179	0.01959	0.04661	0.04464
C_{D_f}	0.00674	0.00573	——	0.01018	——	0.00678	——
C_M	0.00219	−0.00103	−0.00153	−0.00129	−0.00452	−0.01385	−0.00289

[a]See Table 1 for the solutions provided by the listed organizations.
[b]Data without inlet and nozzle surface.

Table A12 Flight condition FC70 force/moment coefficients: statistical analysis[a]

Coefficient	$\hat{\mu}$	$k\hat{\sigma}$	No. of identical solutions	No. of outliers
C_L	0.12276	0.00571	6	1
C_D	0.04193	0.01782	6	1
C_{D_f}	0.00676	0.00357	4	0
C_M	−0.00153	0.00940	6	1

[a]See Table 1 for the solutions provided by the listed organizations.

side force C_Y, rolling moment coefficient C_X, and yawing moment coefficient C_Z. The tables with statistical analysis list the population mean $\hat{\mu}$ and the value $k\hat{\sigma}$ to add/subtract to reach the upper/lower limit that defines the population of identical solutions. It also shows the number of outliers: that is, solutions that are located outside the interval of confidence. The definition of the population mean $\hat{\mu}$ and the value $k\hat{\sigma}$ is in Appendix B.

Appendix B: Statistical Analysis

The forces and moments are statistically evaluated. The use of a statistical approach to analyze collective data is not new [21]: the sequence of AIAA Drag Prediction Workshops used the approach adopted here. The statistical formulas used here are taken from Morrison and Hemsch [21]. The basic idea is to statistically analyze the collective data to evaluate a mean and variance of the solution set and to identify those results that are statistically the same and those that are outliers (i.e., outside of the standard deviation). The population mean $\hat{\mu}$ is estimated using the sample median $\tilde{x}$, which is given (for the sorted data) as

$$\hat{\mu} = \tilde{x} \qquad \tilde{x} \equiv \begin{cases} x_{(n+1)/2} & \text{if } n \text{ is odd} \\ \frac{1}{2}(x_{(n/2)} + x_{(n/2)+1}) & \text{if } n \text{ is even} \end{cases} \tag{1}$$

The sample standard deviation $\hat{\sigma}$ is defined as

$$\hat{\sigma} = \sqrt{\frac{1}{n-1}\sum x_i - \tilde{x}^2} \tag{2}$$

The upper and lower limits for a particular integrated variable (e.g., lift coefficient) define the boundaries for the outliers.

Upper limit:

$$\hat{\mu} + k\hat{\sigma} \qquad k = \sqrt{3} \tag{3a}$$

Lower limit:

$$\hat{\mu} - k\hat{\sigma} \qquad k = \sqrt{3} \tag{3b}$$

Acknowledgments

The authors gratefully acknowledge the support provided by Lockheed Martin Aeronautics Company in providing a refined Integrated Geometry Exchange Package (IGES) geometry file and the parameter values of a generic engine that were subsequently used by facet members in their computational fluid dynamics studies and the geometrical work performed by Edward B. Parlette of Vigyan, Inc., in generating a series of unstructured tetrahedral grids from the IGES file, with the last one known as the base grid. Special thanks also to Todd Michal of Boeing-Phantom Works; Stefan Görtz of DLR, German Aerospace Center; Bruce Davis of Lockheed Martin Aeronautics Company; Willy Fritz of the European Aeronautics and Defence Company, Military Aircraft Systems; David McDaniel of the U.S. Air Force Academy; and Steve Karman of the University of Tennessee for their valuable suggestions and kind assistance in the writing of the paper.

References

[1] Lamar, J. E., Obara, C. J., Fisher, B. D., and Fisher, D. F., "Flight, Wind-Tunnel, and Computational Fluid Dynamics Comparison for Cranked Arrow Wing (F-16XL-1) at Subsonic and Transonic Speeds," NASA TP 2001-210629, Feb. 2001.

[2] Obara, C. J., and Lamar, J. E., "Overview of the Cranked-Arrow Wing Aerodynamics Project International," *Journal of Aircraft*, Vol. 46, No. 2, 2009, pp. 355–368. doi:10.2514/1.34957

[3] Boelens, O. J., Badcock, K. J., Görtz, S., Morton, S., Fritz, W., Karman, S. L., Jr., Michal, T., and Lamar, J. E., "Description of the F-16XL Geometry and Computational Grids Used in CAWAP," *Journal of Aircraft*, Vol. 46, No. 2, 2009, pp. 369–376. doi:10.2514/1.34852

[4] Boelens, O. J., Badcock, K. J., Elmilgui, A., Abdol-Hamid, K. S., and Massey, S. J., "Comparison of Measured and Block Structured Simulations for the F-16XL Aircraft," *Journal of Aircraft*, Vol. 46, No. 2, 2009, pp. 377–384. doi:10.2514/1.35064

[5] Görtz, S., Jirásek, A., Morton, S. A., McDaniel, D. R., Cummings, R. M., Lamar, J. E., and Abdol-Hamid, K. S., "Standard Unstructured Grid Solutions for CAWAPI F-16XL," *Journal of Aircraft*, Vol. 46, No. 2, 2009, pp. 385–408. doi:10.2514/1.35163

[6] Fritz, W., Davis, M. B., Karman, S. L., and Michal, T., "RANS Solutions for the CAWAPI F-16XL Using Different Hybrid Grids," *Journal of Aircraft*, Vol. 46, No. 2, 2009, pp. 409–422. doi:10.2514/1.35106

[7] Boelens, O. J., Spekreijse, S. P., Sytsma, H. A., and de Cock, K. M. J., "Comparison of Measured and Simulated Flow Features for the Full-Scale F-16Xl Aircraft," 45th AIAA Aerospace Sciences Meeting and Exhibit, Reno, NV, AIAA Paper 2007-0489, Jan. 2007.

[8] Michal, T., Oser, M., Mani, M., and Ross, F., "BCFD Unstructured-Grid Predictions on the F- 16XL (CAWAPI) Aircraft," 45th AIAA Aerospace Sciences Meeting and Exhibit, Reno, NV, AIAA Paper 2007-0679, Jan. 2007.

[9] Badcock, K. J., "Evaluation of Results from a Reynolds Averaged Multiblock Code Against F-16XL Flight Data," 45th AIAA Aerospace Sciences Meeting and Exhibit, Reno, NV, AIAA Paper 2007-0490, Jan. 2007.

[10] Elmiligui, A. A., Abdol-Hamid, K. S., and Massey, S. J., "PAB3D Simulations for the CAWAPI F-16XL," 45th AIAA Aerospace Sciences Meeting and Exhibit, Reno, NV, AIAA Paper 2007-0491, Jan. 2007.

[11] Görtz, S., and Jirásek, A., "Unstructured Steady/Unsteady Solutions with Edge for CAWAPI F-16XL at KTH/FOI," 45th AIAA Aerospace Sciences Meeting and Exhibit, Reno, NV, AIAA Paper 2007-0678, Reno, NV, Jan. 2007.

[12] Fritz, W., "Hybrid Grid RANS Solutions For The CAWAPI F-16XL," 45th AIAA Aerospace Sciences Meeting and Exhibit, Reno, NV, AIAA Paper 2007-0492, NV, Jan. 2007.

[13] Karman, S., Mitchell, B., and Sawyer, S., "Unstructured Grid Solutions of CAWAPI F-16XL by UTSimCenter," 45th AIAA Aerospace Sciences Meeting and Exhibit, Reno, NV, AIAA Paper 2007-0681, Jan. 2007.

[14] Lamar, J. E., and Abdol-Hamid, K. S., "USM3D Unstructured Grid Solutions for CAWAPI at NASA LaRC," 45th AIAA Aerospace Sciences Meeting and Exhibit, Reno, NV, AIAA Paper 2007-0682, Jan. 2007.

[15] Morton, S. A., McDaniel, D. R., and Cummings, R. M., "F-16XL Unsteady Simulations for the CAWAPI Facet of RTO Task Group AVT-113," 45th AIAA Aerospace Sciences Meeting and Exhibit, Reno, NV, AIAA Paper 2007-0493, Jan. 2007.

[16] Davis, M. B., Reed, C., and Yagle, P., "Hybrid Grid Solutions on the (CAWAPI) F-16XL Using Falcon v4," 45th AIAA Aerospace Sciences Meeting and Exhibit, Reno, NV, AIAA Paper 2007-0680, Jan. 2007.

[17] Boelens, O. J., "Feature-Based Code Validation Using F-16XL Flight Test and Wind Tunnel Data," NATO Research and Technology Organisation, Oct. 2007, Rept. RTO-MP-AVT-147, Chap. 56.

[18] Cummings, R. M., Morton, S. A., Siegel, S. A., and Bosscher, S., "Numerical Prediction and Wind Tunnel Experiment for a Pitching Unmanned Combat Air Vehicle," 41st Aerospace Sciences Meeting and Exhibit, Reno, NV, AIAA Paper 2003-0417, Jan. 2003.

[19] Jirásek, A., and Rizzi, A., "Numerical Solution for the CAWAPI Configuration on Unstructured Grids at KTH/FOI, Part 2," NATO Research and Technology Organisation, Rept. RTO-TR-AVT-113 Chap. 11 (to be published).

[20] Le Moigne, Y., "Adaptive Mesh Refinement and Simulations of Unsteady Delta-Wing Aerodynamics," Ph.D. Thesis, Royal Inst. of Technology, Farkost och Flygteknik, Stockholm, 2004.

[21] Morrison, J. H., and Hemsch, M. J., "Statistical Analysis of CFD Solutions from the Third AIAA Drag Prediction Workshop," 45th AIAA Aerospace Sciences Meeting and Exhibit, Reno, NV, AIAA Paper 2007-0254, Jan. 2007.